Measurements, wavefunction collapse and dynamics of the quantum impact oscillator

Thesis submitted to IISER Kolkata

for the fulfilment of the requirements for the degree of

Doctor of Philosophy

by

Arnab Acharya

Registration no: 14IP031

Supervisor: Prof. Soumitro Banerjee

Department of Physical Sciences

Indian Institute of Science Education and Research Kolkata

Mohanpur 741 246 INDIA

Declaration

I, **Mr. Arnab Acharya**, with Registration No. **14IP031**, enrolled as a student in the Department of Physical Sciences in the Integrated PhD Programme at IISER Kolkata, declare that this thesis is entirely my own work. I confirm that it does not contain any previously published or written materials by others, and it has not been submitted for any degree, diploma, or academic award elsewhere. To ensure originality, I have utilized an originality-checking service.

I also confirm that any copyrighted material incorporated into this thesis complies with the Indian Copyright Act, 1957 (amended in 2012), and I have obtained written permission from the copyright owners for the use of their work.

I hereby grant IISER Kolkata permission to store this thesis in a publicly accessible database.

Date: February 26, 2024

Arnab Acharya

Arnab Acharya
Department of Physical Sciences
Indian Institute of Science Education and Research Kolkata
Mohanpur 741246, West Bengal, India.

Certificate

I hereby certify that the thesis titled "**Measurements, wavefunction collapse and dynamics of the quantum impact oscillator**", submitted by **Mr. Arnab Acharya**, registration number **14IP031** dated **24th July 2014**, a student of the Department of Physical Sciences in the Integrated PhD Programme of IISER Kolkata is his own and was carried out under my supervision. I confirm that neither the thesis nor any part of it has been previously submitted for any academic degree, diploma, or other academic recognition. In my professional opinion, the thesis meets the requirements for the award of the Doctor of Philosophy degree.

Date: February 26, 2024

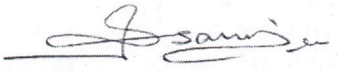

Soumitro Banerjee
Professor
Department of Physical Sciences
Indian Institute of Science Education and Research Kolkata
Mohanpur 741246, West Bengal, India.

Acknowledgements

I want to express my deepest gratitude to my PhD supervisor, Prof. Soumitro Banerjee, for his guidance, support, and exceptional mentorship throughout my doctoral journey. Not only did he equip me with the necessary skills and knowledge in research, but he also inspired in me the true essence of scientific inquiry. I am incredibly fortunate to have had such a remarkable role model who stood by me every step of the way. I owe the completion of this thesis to his relentless efforts in encouraging and motivating me to embrace the challenges of this rigorous academic pursuit.

I would also like to extend my heartfelt appreciation to Bidisha Mukherjee, whose constant presence and support made this journey infinitely better in every aspect. Her belief in me encouraged me to face the hurdles of the PhD journey with courage and determination. Her love and companionship have been my anchor throughout this process.

Furthermore, I am deeply indebted to my family—my mother, father, and sister—for their unshakeable faith in me, even during moments when I doubted myself. My mother, as my first teacher, deserves a special mention. Without her guidance and tireless support, I would not have achieved anything. To my sister, thank you for your love, care, and continuous encouragement. And to my father, thank you for providing me with strength and firm support during the ups and downs of this challenging endeavor.

My time here has been enriched by the presence of some of the most incredible individuals I have had the privilege to meet. Thank you, Saumya Ghosh, for walking this path alongside me and enriching my experience here. I hope you complete your thesis soon. I am immensely grateful, to all my friends at IISER who made this journey enjoyable and memorable. Siddhartha Patra, thank you for the engaging discussions and the wonderful experiences we shared. To my batchmates—Shreya Banerjee, Purba Mukherjee, Tanima Duary, Basabendra Roy, Suvadeep Roy, Debanjana Chakravarty, and Fareeha Saadi—I cannot imagine this experience without your presence.

I would also like to express my gratitude to everyone I shared the NLD lab with for nurturing a warm and supportive atmosphere. Soumyajit Seth,

thank you for your encouragement when I needed it the most. Thank you Subhayu Bagchi, for the stimulating discussions and friendship. Kuntal Mandal, Dhrubajyoti Mandal, and Bichitra Kumar Lenka, your faith in me has been a tremendous source of inspiration. Titir Mukherjee, thank you for all the help and encouragement, it was a pleasure to work on interesting problems with you and I look forward to our joint endeavors. Akhil Bhartiya, thank you for the countless hours we spent together, working on problems and exploring fascinating realms of physics. I am grateful to acknowledge the tireless effort of Akhil, Titir, and Saumya in proofreading this thesis on a tight schedule.

To all those whose names I may not have mentioned explicitly but have played a part in my academic and personal growth, please know that I am profoundly grateful for your contributions.

Finally, I would like to express my sincere appreciation to all the individuals, organizations, and funding agencies who have supported me throughout my research endeavor. Without your generosity, none of this would have been possible.

Thank you all for being integral to this remarkable chapter in my life.

Arnab Acharya

Abstract

This thesis presents an exploration of various aspects of quantum dynamics, collapse mechanisms, and measurement statistics, which collectively contribute to a deeper understanding of quantum behavior. The first chapter investigates the quantum dynamics of a classically chaotic system, revealing a new form of aperiodic wavefunction evolution with strange nonchaotic character. Diagnostic tests confirm this intriguing finding. In the second chapter, statistical properties of periodic measurements on a quantum harmonic oscillator are analyzed, with implications for particle localization accuracy. The third chapter proposes interaction-induced wavefunction collapse models in an impact oscillator, offering testable predictions for energy and position distributions.

Collectively, this research expands our understanding of quantum dynamics. The observed strange nonchaotic behavior opens new avenues for exploring quantum phenomena and potential applications. Proposed collapse models challenge conventional interpretations, offering insights into quantum mechanics' foundations. Statistical analysis of measurements indicated a possibility to control quantum systems. Our findings call for experimental validation, possibly with the supercooled nanomechanical cantilever systems.

Contents

— recommend dividing into 2 sections, or even better, give 1.2.1 - 1.2.6 before Ch. 2 then 1.2.7 - 1.2.13 later (just before Ch. 4?) with 1.2.13 before Ch. 3?

List of Figures

List of Tables

List of Publications

[1] Arnab Acharya, Debapriya Pal, Soumitro Banerjee, and Ananda Dasgupta. Limiting distribution of periodic position measurements of a quantum harmonic oscillator. *Physics Letters A*, 384(18):126397, 2020.

[2] Arnab Acharya, Pratik Jeware, and Soumitro Banerjee. Interaction-induced wavefunction collapse. *arXiv preprint arXiv:2110.03721*, 2021.

[3] Arnab Acharya, Pratik Jeware, and Soumitro Banerjee. Objective collapse induced by macroscopic object. *Foundations of Physics*, 53(4):68, 2023.

[4] Arnab Acharya, Akhil Bhartiya, and Soumitro Banerjee. Signatures of strange nonchaotic dynamics in a forced quantum system. *Physical Review E*, 107(2):024207, 2023.

Chapter 1

Introduction

> I think I can safely say that nobody understands quantum mechanics.
>
> RICHARD PHILLIPS FEYNMAN

1.1 Introduction

Quantum mechanics has a reputation for being elusive and incomprehensible. A century after its inception, physicists still find some of its aspects deeply troubling. The trouble is not mathematical, as is the case for many theories, but conceptual. The working physicist has no trouble calculating predictions for the results of experiments to extreme precision, making it the most well-tested theory to date.

In this thesis, we embark on an exploration of the intricate relationship between chaos, measurement, and collapse mechanisms within the quantum domain. Through investigations on a few different problems, we aim to shed light on some foundational issues. We uncover novel aspects of quantum dynamics, unravel the consequences of interaction-induced collapse, and examine the statistical properties of quantum measurements. By investigating these interconnected threads, we seek to deepen our understanding of the fundamental nature of quantum systems.

Before we embark on this journey, certain notions need to be introduced.

1.2 Theoretical Background

1.2.1 Classical chaos

> But, even if it were the case that the natural laws had no longer any secret for us, we could still only know the initial situation approximately. If that enabled us to predict the succeeding situation with the same approximation, that is all we require, and we should say that the phenomenon had been predicted and that it is governed by laws. But it is not always so; small differences in the initial conditions may produce very great ones in the final phenomena.
>
> JULES HENRI POINCARÉ
> P. 68, Science and Method [1]

In this thesis, a *dynamical system* is any physical system endowed with a state that varies in time according to a deterministic rule. Usually, the state is a point in an N-dimensional *phase space*, $\mathbf{x} \in \mathbb{R}^N$, and the deterministic rule could be an *iterated map*

$$\mathbf{x}_{n+1} = f(\mathbf{x}_n),$$

if time is discrete, or a set of differential equations

$$\dot{\mathbf{x}} = g(t, \mathbf{x})$$

for continuous-time systems, with $f, g : \mathbb{R}^N \to \mathbb{R}^N$. A popular example of a continuous-time dynamical system is the Lorenz system, first introduced by Edward Lorenz in connection with simplified models of atmospheric convection [2]. It is governed by

$$\begin{aligned} \frac{\mathrm{d}x}{\mathrm{d}t} &= \sigma(y - x), \\ \frac{\mathrm{d}y}{\mathrm{d}t} &= x(\hat{\rho} - z) - y, \\ \frac{\mathrm{d}z}{\mathrm{d}t} &= xy - \beta z. \end{aligned}$$

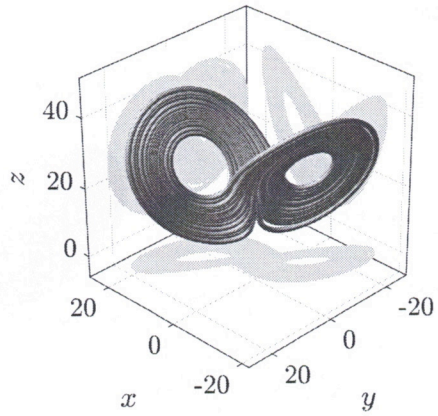

Figure 1.1: A chaotic trajectory of the Lorentz system for the parameter values $\sigma = 10$, $\hat{\rho} = 28$ and $\beta = 8/3$. The trajectory is deliberately made thicker to better illustrate depth. Shadows on the three orthogonal planes show the orthographic projections of the trajectories.

> Does the flap of a butterfly's wings in Brazil set off a tornado in Texas?
>
> EDWARD NORTON LORENZ

For a certain range in parameter values and initial conditions, this system has been shown to exhibit *chaotic dynamics* (Fig. 1.1) in which two nearby initial conditions separate exponentially fast but remain bounded in phase space. The rate of this exponential divergence is called the *Lyapunov exponent* which is defined in Section 1.2.1. Imagine a ball of initial conditions in phase space. The dynamics of the system will stretch and contort the ball after some time. Subsequently, the stretching direction folds, which allows the attractor to remain bounded. This repeated stretching and folding, like kneading of dough, leads to mixing, whereby every initial condition evolves to visit arbitrarily close to every point on the attracting set. Any small difference in initial conditions grows exponentially fast and all predictability is lost. The motion, although perfectly deterministic, looks random, like *chaos*, hence the name. A prerequisite for chaos is the presence of nonlinear terms in the differential equations of motion. For example, the Lorenz system has an xy term in the third equation. Chaos in continuous time systems only occurs for phase space dimension 3 or greater.

Lyapunov Exponents

phase space volume is growing - is energy added to the system?

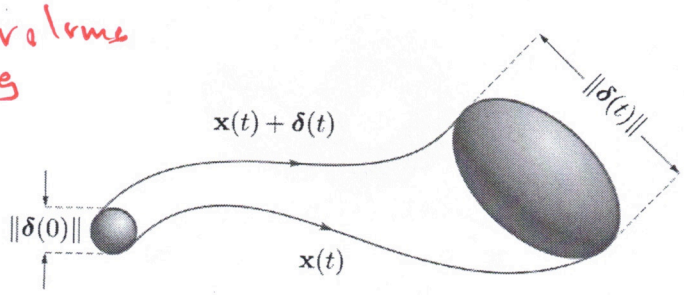

$$\|\boldsymbol{\delta}(t)\| \approx \|\boldsymbol{\delta}(0)\| e^{\lambda t}$$

Figure 1.2: Illustration of Lyapunov exponent. A ball of initial conditions of dimension $\|\boldsymbol{\delta}(0)\|$ is evolved for some time t, and it gets stretched and distorted. This stretching is exponentially fast for chaotic systems. The multiplier in the exponent, λ is called the local Lyapunov exponent for the trajectory. Since the stretching direction folds, the stretching has to be computed over sufficiently small times. Averaging the local Lyapunov exponents over the entire attractor gives us the Lyapunov exponents of an attractor. For an n-dimensional phase space we have n Lyapunov exponents. The direction of the maximum stretch corresponds to the largest Lyapunov exponent. The largest Lyapunov exponent of a chaotic attractor is always positive.

The Lyapunov characteristic exponents of a dynamical system characterize the rate of separation of infinitesimally close trajectories [3]. These exponents are named after the Russian mathematician Aleksandr Lyapunov who pondered the problem of stability of dynamical systems in his Ph.D. thesis [4] and developed a method involving linearization of equations of motion. For a chaotic dynamical system, two nearby initial conditions separated by a distance $\|\boldsymbol{\delta}(0)\|$ in phase space separate exponentially fast (see Fig. 1.2)

$$\|\boldsymbol{\delta}(t)\| \approx e^{\lambda t} \|\boldsymbol{\delta}(t)\| \tag{1.1}$$

at an exponential rate given by λ. For a dynamical system with an n-dimensional phase space, these rates of separation can be different for different orientations of the initial distance vector. Hence, there exists a spectrum of Lyapunov exponents equal in number to the dimension of the phase space. In general, the spectrum is different for different initial conditions, but generally, we are interested in the values of these exponents averaged over an attractor. The largest of these exponents, $\lambda_{\max}$ determines whether the system is regular ($\lambda_{\max} \leq 0$) (periodic, quasiperiodic) or chaotic ($\lambda_{\max} > 0$).

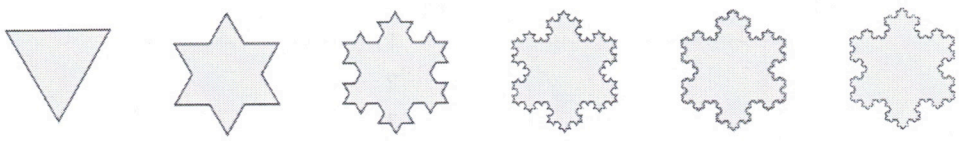

1 2 3 4 5 ∞

Figure 1.3: The iterative process of generating the Koch snowflake, named after the Swedish mathematician Helge von Koch [25]. Begin with an equilateral triangle. Taking the middle third of each side as a base, construct smaller equilateral triangles on each side. Now remove the base. Repeating this process ad infinitum gives us a snowflake-like structure. Notice that each step increases the perimeter by a factor of 4/3. The area on the other hand, increases additively in the series $A_1(1 + 1/3 + 1/3^2 + \ldots + 1/3^n + \ldots)$ which adds up to $3A_1/2$. So, in the limit of infinite steps, its length approaches infinity but its area remains finite.

Henceforth, by Lyapunov exponent, we shall refer to the largest exponent. Several methods have been developed to reliably compute the Lyapunov exponent from time series data [5–19].

In dissipative dynamical systems, where there is a continuous loss of energy, the state often evolves towards stable structures in phase space. These stable sets are called *attractors* as they attract all trajectories in their neighborhood towards them. An attractor is said to be *strange* if it has a *fractal* structure. Fractals are described in the following section. Strange attractors typically occur in dissipative chaotic systems (see Fig. 1.1), but *strange nonchaotic attractors* also exist [20]. These attractors are strange in the sense of being geometrically fractal, but their largest Lyapunov exponent is negative. Such attractors have been typically found to occur in *quasi-periodically* driven dissipative systems [21], [22], [23]. A quasi-periodic drive is one composed of two or more incommensurate frequencies. Systems without external drive can also have strange nonchaotic dynamics. Remarkably, certain stars pulsating at the golden ratio have shown signs of strange nonchaotic attractors [24].

Fractals

Fractals are geometrical objects that have detailed structures at all scales. They are neither a finite set of points nor piecewise-differentiable. An example of a fractal is the Koch snowflake (Fig. 1.3). Although they are often self-similar under scaling, it is not a strict requirement. Rather, fractals are characterized by their fractal dimension. Unlike smooth objects which have

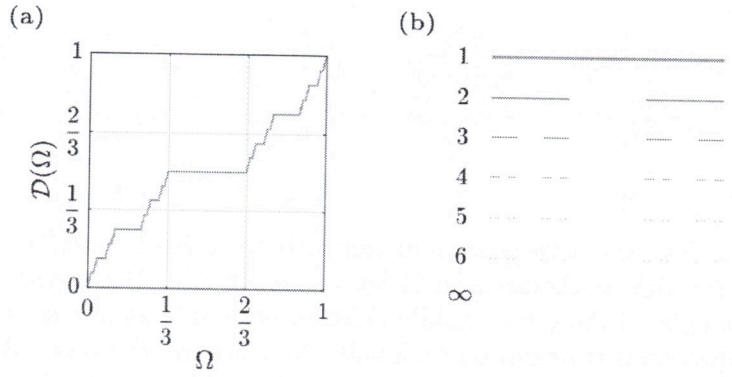

Figure 1.4: (a) A devil's staircase is a continuous, monotonically increasing function that is differentiable almost everywhere with derivative zero, except on a Cantor set. Functions with this property are called *singular*. Its devious character lies in the fact that an infinite number of steps lead only to a finite ascent. (b) The middle-thirds Cantor set is a fractal that is formed by removing the middle thirds of a segment of unit length. The two resulting segments are subjected to the same procedure. Repeating this process *ad infinitum* generates the Cantor set. The Cantor set is a fractal with self-similar properties at all scales. The *fractal dimension* of this set is $\log 2/\log 3 \sim 0.69$. See Section 1.2.1 for the definition of fractal dimension. This particular devil's staircase is called Cantor's function. Notice that the devil's staircase is constant on intervals where the middle-thirds Cantor set is empty.

integer dimensions, fractals possess fractional dimensions. The concept of dimension is intuitively related to how the bulk of something scales as its size is changed. For example, when we double the sides of a cube, its volume increases eight-fold which is 2^3. Hence, the dimension of the cube is 3. This intuitive notion can be formally written down as [26]

$$\text{dimension} = \lim_{\text{size}\to 0} \frac{\log(\text{bulk})}{\log(1/\text{size})}. \tag{1.2}$$

The small size limit entails that dimension is a local property and extending it to a global notion will require some form of averaging where the measured dimension is different in different parts of the structure. The concept of dimension is intimately related to the degrees of freedom in the set. A rigorous definition of dimension was given by Hausdorff [27] but the definition is not operationally applicable. Hence, several alternative estimates of the dimension of a geometrical object have been developed. For instance,

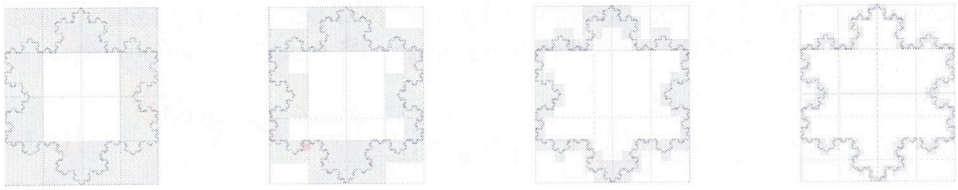

$\frac{\log 12}{\log 4} \approx 1.7925$ $\frac{\log 36}{\log 8} \approx 1.7233$ $\frac{\log 87}{\log 16} \approx 1.6107$ $\frac{\log 216}{\log 32} \approx 1.5510$

Figure 1.5: An illustration of the box-counting dimension for the Koch snowflake. As the grid gets finer the approximation of the dimension gets better. The limiting value is $\ln 4/\ln 3 \approx 1.2619$.

the *pointwise dimension* is a measure of the dimension around a point on an attractor. For a pointwise mass function $B_{\mathbf{X}}(r)$ defined for a ball $\mathcal{B}_{\mathbf{X}}(r)$ of radius r centered at $\mathbf{X}$ as

$$B_{\mathbf{X}}(r) = \mu[B_{\mathbf{X}}], \tag{1.3}$$

the pointwise dimension at $\mathbf{X}$ measures the scaling of this mass function at $\mathbf{X}$ with r

$$D_p(\mathbf{X}) = \lim_{r \to 0} \frac{\log B_{\mathbf{X}}(r)}{\log 1/r} \tag{1.4}$$

To extend it to a global dimension for an attractor, $\mathcal{A}$, a weighted averaging is performed

$$D_p = \int_{\mathcal{A}} D_p(\mathbf{X}) \mu(\mathbf{X}). \tag{1.5}$$

A computationally simpler dimension is the *box-counting/ capacity dimension*. For a finite-sized grid of size r, it is defined as

$$D_c = \lim_{r \to 0} \frac{\log n(r)}{\log 1/r} \tag{1.6}$$

where $n(r)$ is the number of boxes in the grid that have some part of the object in it. It provides an upper bound for the Hausdorff dimension which gets tighter as the size of the grid size r is reduced. An illustration of calculating the box-counting dimension for the Koch snowflake is provided in Fig. 1.5.

While calculating the box-counting dimension, each box was either counted or discarded based on the presence or absence of the object in it. But any information about the number of points in a box was thrown away. The *generalized dimension* takes this into account by counting the number of

points in the i^{th} box and dividing it by the total number of points to find the probability P_i of the attractor being in the i^{th} box. It is defined as

$$D_q = \frac{1}{q-1} \lim_{r \to 0} \frac{\log \sum_i P_i^q}{\log r} \quad (1.7)$$

The value of q determines the kind of averaging. For $q = 2$, it is the arithmetic average, while for $q = 3$ it is the root mean square average. $q \to 1$ tends to be the geometric average. The generalized dimension was first developed out of a need to explain why different algorithms gave different results for the dimension of a fractal set. For uniform fractals, D_q does not vary with q which ascribes a unique dimension to the fractal. For nonuniform fractals, D_q increases with increasing q and the dimension of the fractal is a spectrum of values between $D_{-\infty}$ and $D_{-\infty}$.

The measured fractal dimension can be different at different parts of the object, or different scales. Such objects are called *multifractals*.

Characterizing attractors

Strange attractors have a fractal structure so they can be characterized by computing their fractal dimensions. Other methods of characterizing attractors have also been developed.

The *Lyapunov dimension* is specifically a way of characterizing the dimension of a strange attractor. It is defined as [28]

$$D_L = j + \frac{1}{|\lambda_{j+1}|} \sum_{i=2}^{j} \lambda_i \quad (1.8)$$

where j is the highest index for which the sum $\sum_{i=2}^{j} \lambda_i$ is non-negative.

Yet another measure of dimension comes from how much information is required to specify a fractal at a certain scale. Its scaling with size leads to the *information dimension* [28]

$$D_I = -\lim_{\epsilon \to 0} \frac{I(\epsilon)}{\ln 1/\epsilon}, \quad (1.9)$$

where

$$I(\epsilon) = -\sum_{i=1}^{N_\epsilon} p_i \ln p_i. \quad (1.10)$$

Different types of attractors in dynamical systems

In dissipative dynamical systems, a phase space trajectory moves from one energy shell to the next as it dissipates energy. As energy shells, like Russian dolls, are contained within one another from the larger to the smaller, this leads to shrinkage in phase space volumes. If this decrease is allowed to happen without bound, the system will asymptotically approach a stable equilibrium point. However, if the system has a source of energy, the competition between the two opposing forces leads to rich and interesting dynamics. The phase space trajectories can asymptotically approach structures which can be points, called *fixed points*, periodic orbits, called *limit cycles*, or meander around aperiodically approaching but never quite reaching bounded sets which are fractals.

Such geometrically nontrivial attractors with non-integer fractal dimension and Cantor set structure are called *strange attractors*, coined first by Ruelle and Takens in [29]. Before chaos theory had matured, Edward Lorenz, faced with this monstrosity, tried to describe it as "... an infinite complex of surfaces, each extremely close to one or the other of two merging surfaces." [2]. The dynamics on these attractors are typically extremely sensitive to the initial conditions of the trajectory, such that two very close initial conditions spread away exponentially fast. But because the attractor is bounded, this divergence cannot continue indefinitely, eventually reaching the size of the attractor and then recurrently coming closer and moving apart. fixed point, limit cycle, High periodic limit cycle, quasiperiodic, mode-locked periodic, strange attractor-chaotic, and nonchaotic.

The set of all states that eventually evolve to a certain attractor is called the *basin of attraction* of that attractor. The basin of attraction of a magnetic pendulum is illustrated in Fig. 1.6.

1.2.2 Strange Nonchaotic Attractors (SNA)

Although strange attractors are typically chaotic, this behavior is not universal, as was first demonstrated by Grebogi *et al.* in systems driven quasiperiodically (at two incommensurate frequencies) [20]. These special attractors, called Strange Nonchaotic Attractors, or SNA for short, were later found to be quite commonplace in quasiperiodically driven systems, generally appearing in parameter space, at the edge of periodicity/quasiperiodicity and chaos. Their dynamics are also in a sense intermediate between regular and chaotic—no sensitive dependence on initial conditions, yet aperiodic, with a fractal structure, like chaotic systems.

SNAs have been found to occur in quasiperiodically driven magneto-

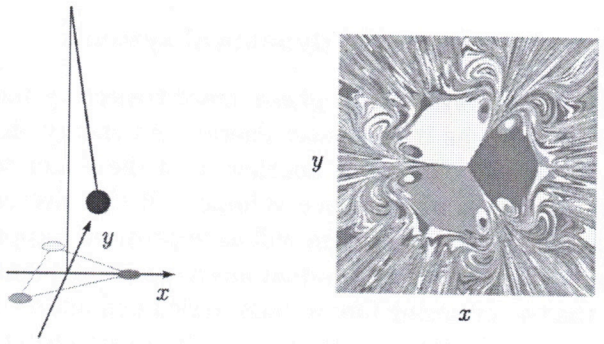

Figure 1.6: A magnetic pendulum consists of a bob made of iron suspended from a pivot about which it can swing freely. Three magnets are placed at three corners of an equilateral triangle on a horizontal surface. The magnets are strong enough that the gravitational stable equilibrium point becomes unstable and three new stable equilibria, corresponding to each magnet, are born. The basin of attraction for these three equilibrium points is plotted in color. The basin boundary forms a fractal structure which gives rise to the extreme sensitivity to initial conditions in this system. This figure is adapted, with slight modification, with permission from [30].

elastic ribbons [31], electrochemical cells [32], electronic circuits [33–36], overdamped Josephson junctions [37], pendula [38], Ueda's circuit [39], in the piecewise-smooth articulated mooring tower model [40], and in several discrete-time maps [38, 41–45]. Digital and analog simulations of a multistable potential with quasiperiodic drive, which models a radio-frequency-driven superconducting quantum interference device (SQUID) with inertia and damping effects, have found SNAs that are robust to noise inherent in realistic devices [46]. Simulations of the Shimizu-Morioka oscillator also shows signs of SNAs [47]. A circuit with two LCR oscillators, driven sinusoidally and coupled to each other by a nonlinear element with piece-wise linear v-i characteristics was shown to exhibit strange nonchaotic dynamics [48]. Sathish *et al.* have demonstrated the presence of strange nonchaotic attractor in a periodically driven Duffing oscillator in the presence of noise. SNAs have also been observed in neon glow discharge without any external forcing [49]. An intriguing discovery was finding strange nonchaotic attractors in data collected by the *Kepler* spacecraft [24]. These star systems, whose brightness oscillations have primary and secondary frequencies in the golden ratio, show signatures of SNAs.

An unexpected connection exists between SNAs in classical systems and spatially quasiperiodic potentials in quantum systems. This equivalence was

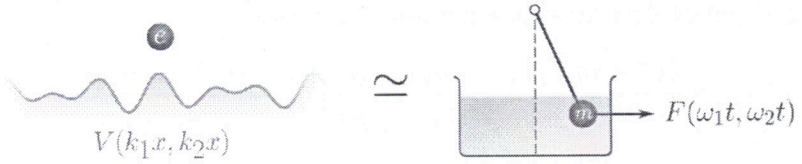

Figure 1.7: The quantum dynamics of an electron in a quasiperiodic potential is isomorphic to a strongly damped driven pendulum (in this illustration, the bob is submerged in a highly viscous fluid). This correspondence, which comes about through the Prüfer transformation, has interesting consequences for both systems. In particular, when driven at two incommensurate frequencies, the dynamics of the pendulum becomes strange nonchaotic and the quantum spectrum becomes fractal.

first elucidated by Bondeson *et al.* [50] for the time-independent Schrödinger equation,

$$\psi'' + \lambda V(x)\psi = E\psi, \tag{1.11}$$

where $V(x)$ is spatially quasiperiodic, $V(x) = \sin k_1 x + \sin k_2 x$ (Fig. 1.7). Such potentials are studied extensively [51–53] because of their relevance to condensed matter physics and also because they lie somewhat between periodic crystals where the quantum states are delocalized Bloch waves [54] and random disordered materials where the states are Anderson localized [55]. For irrational values of k_1/k_2 and small λ the energy eigenstates are typically extended while for large λ the states are typically localized. The energy spectrum is known to lie on a Cantor set (see Fig. 1.4(b)) of finite measure with stop-bands lying on the complement of this Cantor set [56–59]. One applies the Prüfer transformation $\psi(x) \to \phi(x)$ via

$$e^{i\phi} = \frac{\psi' + ig\psi}{\psi' - ig\psi}, \tag{1.12}$$

where g is an arbitrary constant. Using Euler's formula to expand the exponent in the left-hand side, grouping the real and imaginary terms on the right-hand side, and assuming that ψ to be real, we obtain

$$\cos\phi + i\sin\phi = \frac{\psi'^2 - g^2\psi^2}{\psi'^2 + g^2\psi^2} + i\frac{2g\psi\psi'}{\psi'^2 - g^2\psi^2}. \tag{1.13}$$

Comparing real and imaginary terms on both sides,

$$\cos\phi = \frac{\psi'^2 - g^2\psi^2}{\psi'^2 + g^2\psi^2}, \quad \text{and} \quad \sin\phi = \frac{2g\psi\psi'}{\psi'^2 - g^2\psi^2}. \tag{1.14}$$

Taking a spatial derivative of equation 1.12 yields

$$e^{i\phi}i\phi' = \frac{(\psi'' + ig\psi')(\psi' - ig\psi) - (\psi' + ig\psi)(\psi'' - ig\psi')}{(\psi' - ig\psi)^2}. \tag{1.15}$$

Substituting $e^{i\phi}$ from equation 1.12 and simplifying the right hand side, we obtain

$$\frac{\psi' + ig\psi}{\psi' - ig\psi}i\phi' = 2ig\frac{\psi' - \phi''\psi}{(\psi' - ig\psi)^2} \tag{1.16}$$

or,
$$\phi' = 2g\frac{\psi'^2 - \psi''\psi}{\psi'^2 + g^2\psi^2}. \tag{1.17}$$

Substituting ψ'' from equation 1.11,

$$\phi' = 2g\frac{\psi'^2 + (E - \lambda V)\psi}{\psi'^2 - g^2\psi^2}, \tag{1.18}$$

rearranging terms in the numerator

$$\phi' = \frac{\left(g - \frac{E-\lambda V}{g}\right)(\psi'^2 - g^2\psi^2) + \left(g + \frac{E-\lambda V}{g}\right)(\psi'^2 + g^2\psi^2)}{\psi'^2 + g^2\psi^2} \tag{1.19}$$

$$= \left(g - \frac{E - \lambda V}{g}\right)\frac{\psi'^2 - g^2\psi^2}{\psi'^2 + g^2\psi^2} + \left(g + \frac{E - \lambda V}{g}\right), \tag{1.20}$$

and substituting by $\cos\phi$ from equation 1.14 and simplifying, we reach our desired equation

$$\phi' = \frac{1}{g}\left[\left\{g^2 - E + \lambda V(x)\right\}\cos\phi + \left\{g^2 + E - \lambda V(x)\right\}\right]. \tag{1.21}$$

This can be shortened to

$$\phi' = \alpha(x)\cos\phi + \beta(x). \tag{1.22}$$

This is the same as the equation of motion of a highly damped driven pendulum

$$\nu\dot{\theta} = \gamma(t)\cos\theta + f(t), \tag{1.23}$$

where the angle ϕ is measured with respect to the horizontal direction and ν, γ, and f represent the frictional, gravitational and external torques respectively. The inertial term $\ddot{\phi}$ has been neglected, which is appropriate in the case of very high damping and slow-varying $\gamma(t)$ and $f(t)$ functions.

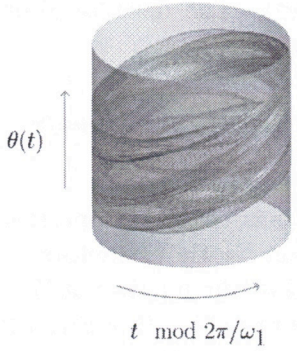

Figure 1.8: A heavily damped pendulum driven quasiperiodically at two incommensurate frequencies $f(t) = \cos\omega_1 t + \cos\omega_2 t$ has strange nonchaotic dynamics. The attractor for the system is shown. The time variable is wrapped around with the period of the first forcing frequency resulting in the whole dynamics being confined on a cylinder.

It was shown in [50], that after a suitable coordinate transformation, the Lyapunov exponent and the *winding number* of the solutions of equation 1.22 and equation 1.23 are the same upto a constant value, thus establishing the connection between the two systems. Furthermore, as a parameter is varied, Bondeson *et al.* show that the winding number increments form a *devil's staircase* (see Fig. 1.4(a)). This pendulum system has been shown to exhibit a three-frequency quasiperiodic orbit, a two-frequency quasiperiodic attractor, and strange nonchaotic behavior which correspond to spatially extended, stop-band, and localized solutions of the Schrödinger equation. The strange nonchaotic attractor for the pendulum system is shown in Fig. 1.8.

Detection and characterization of SNAs

SNA detection from experimental time series involves two steps – (1) to show that the time series is not chaotic, the Lyapunov exponent must be non-positive and (2) to uncover the geometrical character of the attractor, the fractal dimension, and scaling properties of the spectral distribution are estimated. Detection of SNAs from experimental time series or numerical simulation requires that its two characteristic features–(i) its strange attractor, and (ii) its non-chaotic behavior, be established.

Power spectral features: The discrete Fourier transform [60] of the samples of a time series $\{x_n\}$ given by

$$X_k = \sum_{n=1}^{N} x_n e^{-2\pi i n k/N} \tag{1.24}$$

for the k-th Fourier mode has scaling properties that can be utilized for the detection of strange nonchaotic attractors. The spectral distribution function $N(\sigma)$[61] is defined as the number of Fourier peaks with amplitude greater than an arbitrary threshold σ (see Fig. 1.9(a) and (b)). For strange nonchaotic attractor it was shown that the spectral distribution function scales like a power-law

$$N(\sigma) \sim \sigma^{-\alpha}, \tag{1.25}$$

whereas for two-frequency and three-frequency quasiperiodic attractors it scales as $\ln 1/\sigma$ and $\ln^2 1/\sigma$ respectively.

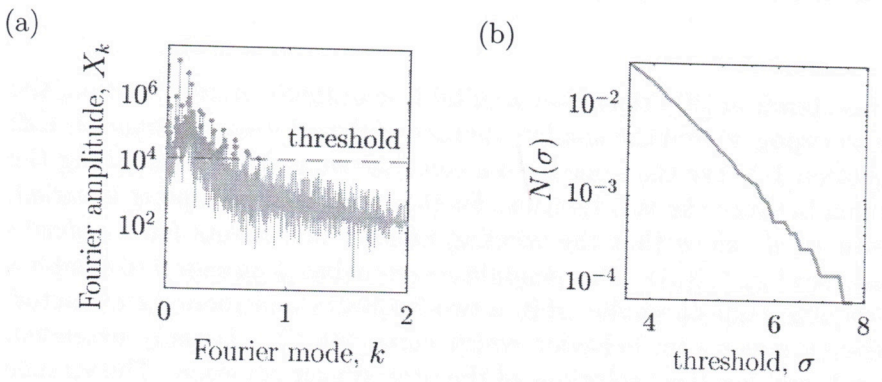

Figure 1.9: (a) An illustration of the process of calculating the scaling (b) spectral distribution function

Density of finite-time Lyapunov exponents: Although the average Lyapunov exponent on a strange nonchaotic attractor is negative, local instabilities due to the strangeness give rise to a positive Lyapunov exponent when calculated on shorter fragments of the time series. Here 'short' refers to fragments whose time duration is shorter than the fundamental period of the dynamics. These are called finite-time Lyapunov exponents (FTLEs). These regions of positive FTLEs are compensated by larger regions on the attractor having negative FTLEs. This property can be used as a distinguishing feature of SNAs. The stationary density of FTLEs, defined such that $P(N, \lambda)d\lambda$ is the probability that a chunk of time series of length N has

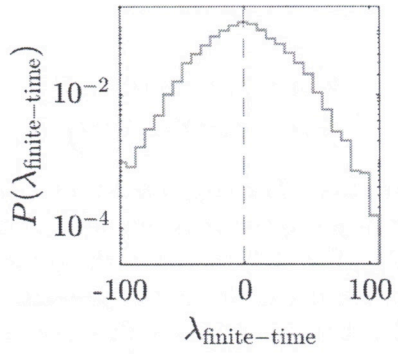

Figure 1.10: Stationary density of finite-time Lyapunov exponents for a typical system with strange nonchaotic dynamics.

FTLE which lies between λ and $\lambda + d\lambda$ [62, 63]. The local instabilities in SNAs result in the density of FTLEs having some component at positive λ. This component decreases as N is increased. An example of such a density is plotted in Fig. 1.10.

Fractal dimension of the attractor: A strange attractor is a fractal object. Hence estimating its fractal dimension (see Section 1.2.1) is a straightforward method to characterize the strangeness of an attractor. A long-standing conjecture by Kaplan and Yorke [64–66] suggests the equality of the Lyapunov dimension and the information dimension. If it is valid in the case of strange nonchaotic attractors, it would imply that $D_L = D_I = 1$. This can be used to distinguish SNA from chaotic attractors for which D_I is expected to be larger than 1. The conflicting local and global stability features of strange nonchaotic attractors make the estimation of their dimension numerically difficult requiring a large number of points for modestly accurate estimation [67].

The 0-1 test: The 0-1 test was proposed by Georg A. Gottwald and Ian Melbourne in a series of papers [68–70]. Originally intended to distinguish between periodic/quasiperiodic and chaotic time series, it has found wider application as it has the advantages of not requiring phase space reconstruction [71], being computationally inexpensive and easy to implement. It takes a sampled data set as input and outputs a single value, K, between 0 and 1, with 0 indicating periodicity/quasi-periodicity and 1 indicating chaos. No prior information about the system is required to apply the test.

The given time series ϕ_n for $n \in \mathbb{N}$ is used to drive the two dimensional

system

$$p_{n+1} = p_n + \phi_n \cos cn, \tag{1.26}$$
$$q_{n+1} = q_n + \phi_n \sin cn, \tag{1.27}$$

where $c \in (0, 2\pi)$ is a constant. For large classes of systems, it can be shown that [72] the trajectory in $p - q$ plane is bounded if the driving time series is periodic/quasi-periodic (Fig. 1.11(a)). On the other hand, the trajectory is asymptotically Brownian if the driving time series is chaotic and grows diffusively (Fig. 1.11(b)). The mean square displacement

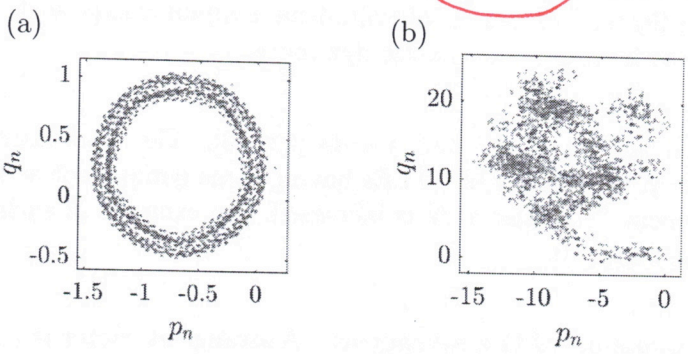

Figure 1.11: The iterates (p_n, q_n) when forced with (a) regular time series, saturate at a certain distance from the origin. (b) When forced with a chaotic time series, however, it grows diffusively akin to a 2-dimensional random walk.

$$M_n = \frac{1}{N} \sum_{j=1}^{N} \left[(p_{j+n} - p_j)^2 + (q_{j+n} - q_j)^2 \right] \tag{1.28}$$

grows linearly in the case of chaotic time series and saturates for regular time series. Typically values of M_n are calculated for $n < N/10$ to ensure the $N \to \infty$ limit. This asymptotic growth rate of the mean square displacement is distilled into a diagnostic, K given by

$$K = \lim_{n \to \infty} \frac{\log M_n}{\log n} \tag{1.29}$$

which gives the value $K \approx 0$ for a periodic/quasiperiodic time series and $K \approx 1$ for a chaotic time series. The value of $c \in (0, 2\pi)$ is chosen randomly, as resonances with the internal frequencies $c = \omega$ can lead to spurious resonances

and give a misleading result. The computation is hence repeated for several values of c and the median K value is the final result. The test can suffer from oversampling and finite-size effects, but steps to overcome both are mentioned in [73, 74]. Mathematical justification for these claims can be found in [72, 75].

If the $p-q$ system is driven by a time series from a strange nonchaotic attractor, the mean square displacement is seen to grow slower than diffusively but never saturate[76]. Gopal *et al.* [77] have extended the 0-1 test to work reliably in distinguishing strange nonchaotic attractors from other forms of dynamics by fixing the value of c to the golden ratio $\left(\sqrt{5}+1\right)/2$. Toker *et al.* [78] have devised a pipeline for the detection of chaos which used the 0-1 test. They have demonstrated that the test can successfully distinguish between strange-nonchaotic attractors and chaos among other things.

The following two methods have also been proposed by some authors. However, for our work, we did not use them.

Parameter and phase sensitivity: A strange attractor is a non-differentiable object (in directions other than that of the trajectory) with structures down to indefinitely small scales. This non-differentiability was utilized in [63] to distinguish between smooth and strange attractors. The maximum value of the derivative of a strange attractor $x(\theta)$ with respect to the external phase of forcing, $dx/d\theta$ was shown to grow boundlessly. The phase sensitivity function

$$\Gamma_N(x,\theta) = \min_{x,\theta}\left[\max_{0\le n\le N}\left|\frac{\partial x_n}{\partial \theta}\right|\right] \tag{1.30}$$

measures the growth rate of the derivative with respect to the external phase as the length of the time series, N increases. For the case of chaotic attractors, this grows exponentially with N [79]. For SNA, the growth is a power law [63, 80]

$$\Gamma_N \sim N^{\mu}. \tag{1.31}$$

Phase sensitivity has been generalized to higher dimensions in [81]. Other measures may be devised based on similar ideas. For instance, the integral of the derivative $dx/d\theta$ converges for a smooth curve, while it diverges for strange attractors. Along similar lines, sensitivity to the variation of a parameter ϵ may be quantified as

$$\Gamma^{\epsilon}_N = \min_{x,\theta}\left[\max_{0\le n\le N}\left|\frac{\partial x_n}{\partial \epsilon}\right|\right], \tag{1.32}$$

which also shows power law growth for strange nonchaotic attractors [80].

Autocorrelation function: Pikovsky *et al.* used the autocorrelation function to study the characteristic features of SNA [82]. The autocorrelation function for a discrete time series with zero-mean is defined as

$$R(\tau) = \frac{\langle x_t x_{t+\tau} \rangle}{\langle x^2 \rangle}. \tag{1.33}$$

They find that for a quasiperiodic orbit, R never reaches the value 1 although it comes arbitrarily close to 1 at resonant times. For SNA they report self similarity near resonant times with peaks of height halfway between 0 and 1. The mean squared autocorrelation

$$R_{\text{av}} = \frac{1}{t} \sum_{\tau=1}^{t-1} |R(\tau)|^2 \tag{1.34}$$

decays exponentially for chaotic motion, but hovers around intermediate values for SNA [79].

1.2.3 Hamiltonian chaos

In Hamiltonian systems, which conserve energy, chaos shows up in a slightly different form. The phase space is mixed, with parts of it being chaotic and other parts periodic or quasi-periodic. For Hamiltonian systems with a $2n$-dimensional phase space, having n constants of motion makes them *integrable*. In such systems, the dynamics is confined to an n-dimensional torus. Kolmogorov, Arnold, and Moser studied the persistence of such tori under small perturbations. The KAM theorem, which bears their names, states that under small perturbations, some of the tori survive. The union of all surviving tori is called the Kolmogorov set, on which the dynamics is quasiperiodic. In the complement, the dynamics can be very complicated. Chaotic islands are enveloped by KAM-tori. The evolution preserves phase space volume, hence there are no attractors, but the Lyapunov exponent continues to be positive for chaotic systems. A few aspects of chaos in Hamiltonian systems will be illustrated in the context of a kicked rotor system in a subsequent section.

1.2.4 Quantum chaos

One of the prominent realizations of this century has been that the world is inherently quantum. Quantum theory has successfully fended all the experimental scrutiny we have been able to throw at it. Macroscopic quantum

effects like superconductivity and superfluidity have us convinced that quantum mechanics is not just confined to the scale of atoms and molecules. It follows then that classical mechanics must be an approximation to the underlying quantum description. Nevertheless, even a century after its inception, we are at a loss to explain features of the classical world in terms of quantum principles except for very simple model systems.

One of the pressing questions in this *quantum to classical transition* is: How do we explain the appearance of chaos in classical systems from quantum principles? The linear quantum dynamics of the Schrödinger equation is inadequate to explain the appearance of sensitive dependence on initial conditions in classical systems. The only nonlinearity in the quantum description comes through the process of measurement, which can and has been used to explain the appearance of chaos [83–86], but it comes with its own baggage of problems as we will discuss in a later section (Section 1.2.7).

Remarkable as it is, this inability to explain deterministic chaos from quantum principles was not the first brush between chaos theory and quantum mechanics. Borrowing an insight from Poincaré, Einstein extended the old quantum theory of Bohr, Sommerfeld, and Epstein, which is popularly known today as the Wentzel-Kramer-Brillouin (WKB) method, to include classical systems where the motion is on a torus. This is known today as Einstein–Brillouin–Keller (EBK) quantization. Einstein could grasp that even his slightly generalized quantization condition fails when the number of integrals of motion is less than the number of degrees of freedom [87].

The new quantum theory of Schrödinger and Heisenberg could accommodate such systems, but newer questions emerged. Would Bohr's *correspondence principle*—which claimed that classical laws should arise in appropriate limits of quantum laws, hold for systems whose classical limits are chaotic? How can quantum dynamics, governed by the linear Schrödinger equation give rise to the appearance of nonlinearity and deterministic chaos in the classical world? It turned out that deterministic chaos, in its usual sense, is ruled out because of the linear nature of quantum evolution [88]. The overlap between two states, which measures the similarity between two states, is an invariant of the quantum dynamics

$$\langle\psi(0)|\phi(0)\rangle = \langle\psi(0)|\,\hat{U}^\dagger\hat{U}\,|\phi(0)\rangle = \langle\psi(t)|\phi(t)\rangle\,. \tag{1.35}$$

Yet, classically chaotic systems do show distinct signatures in their quantized counterparts [89]. Although quantum dynamics shows no sensitive dependence on initial states, the expectation values of the commutators of local operators, called the out-of-time-order correlators do capture the exponential divergence seen in the classical counterpart [90–94]. A small number

of eigenstates of such classically chaotic systems have enhanced probability density around classically periodic orbits, a fact known as *scarring*, leading to weak ergodicity breaking [95–97]. The study of such signatures has led to a large body of knowledge giving birth to the field of quantum chaos [98–100]. Some of these developments will be illustrated using the specific case of the kicked rotor in the subsequent section.

The kicked rotor

Over the past half-century, the kicked rotor (Figure 1.12(a)) has emerged as a highly influential model that has made significant contributions to the theoretical developments in the field of quantum chaos [101]. From a classical perspective, this rotor serves as a natural model for several compelling reasons. Its structural characteristics align with generalized coordinate systems, particularly the action-angle variables, which are fundamental for understanding the dynamics of integrable systems. In these action-angle coordinates, integrable dynamics resemble the motion of a free particle within a cylindrical phase space, where the position coordinate takes on the characteristics of an angle.

This system provides a valuable framework for exploring how perturbations can disrupt integrability and nearly-integrable dynamics. It has played a pivotal role in research related to the Kolmogorov-Arnold-Moser (KAM) theory, which investigates how quasi-periodic motion in integrable systems either persists or disintegrates due to perturbations. The kicked rotor features a control parameter (the kicking strength) that determines the nature of its dynamics. At lower parameter values, the system remains integrable or close to it, but as the parameter increases, the system undergoes a transition towards fully developed and strongly chaotic dynamics.

There are two primary versions of the kicked rotor, each with distinct applications. The first version exhibits an infinite cylinder in phase space. Its dynamics in the momentum variable display a range of behaviors, from confined dynamics in the integrable and nearly-integrable regimes to diffusion in the fully chaotic regime [102]. In between, it showcases combinations of confined dynamics, diffusion, and accelerator modes, which exhibit rapid energy growth. Various crucial quantities, such as diffusion constants, action diffusion constants, and Lyapunov exponents, can be computed analytically. Other aspects, such as determining the parameter value at which the last KAM torus breaks down, have been the subject of extensive study.

The second version of the kicked rotor, periodic in momentum, forms a torus in phase space, which is compact and finite in extent (Figure 1.12(b)). Here, dynamics can vary from integrable to chaotic, but momentum diffusion

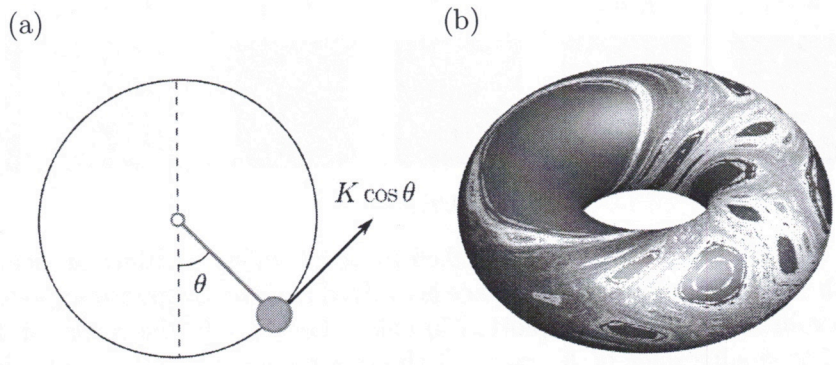

Figure 1.12: (a) A schematic diagram of the kicked rotor system. The rotor rotates with constant angular momentum p except at periodic instants when the momentum is kicked by an amount $K\cos\theta$ where θ is the instantaneous phase of the rotor and K is the kicking strength. This system is a paradigmatic example of chaos in Hamiltonian systems both in classical and quantum mechanics. (b) The phase space of the momentum-bounded kicked rotor system lives naturally on a torus. The colors correspond to the Lyapunov exponents of the trajectories residing in those regions.

cite source or did he create this? (applies to a many figs in this section)

is no longer possible. This version is more suitable as a model for bounded systems, whereas the former version primarily serves open systems.

In the realm of quantum mechanics, quantizing the kicked rotor on a cylinder is straightforward as has been shown in the following section. It has been associated with a Lloyd model of Anderson localization, and the localization properties of its eigenfunctions have been extensively explored across various regimes. The presence of a reflection symmetry around zero momentum produces a new kind of tunneling between the Anderson localized eigenstates. The kicked rotor has played a pivotal role in studies concerning the quantum suppression of classical behavior, quantum accelerator modes, and more recent explorations related to fidelity. Additionally, it has enhanced our understanding of the statistical characteristics of extreme values associated with eigenangles and eigenvectors and their implications for quantum entanglement and quantum information theory.

The classical kicked rotor

A general kicked rotor pertains to a particle constrained to move along a circular path and is subjected to instantaneous kicks at time intervals of $n\tau$. If we consider the radius of the circular path as $1/2\pi$ and τ as 1, the

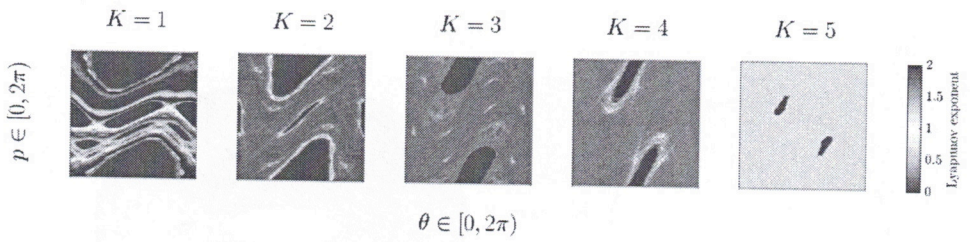

Figure 1.13: Phase portrait of the kicked rotor for different values of kicking strength K. Each point in phase space is evolved and the Lyapunov exponent of the evolution trajectory is plotted in color. For $K = 0$, the rotor rotates freely. For small values of K, parts of the phase space become chaotic but these are restricted by invariant tori. At the critical value $K \approx 0.97$ the last invariant torus is destroyed.

corresponding Hamiltonian takes the following form:

$$H(\theta, p) = \frac{p^2}{2} + V(\theta) \sum_{n \in \mathbb{Z}} \delta(t - n) \tag{1.36}$$

Here, $V(\theta)$ represents a function that exhibits periodic behavior within the range $\theta \in [0, 2\pi)$. From the Hamiltonian $H(\theta, p)$, we can derive mapping equations that establish the connection between the position and momentum (θ_{i+1}, p_{i+1}) of the particle just before the $(n+1)$th kick and those (θ_i, p_i) just before the nth kick as follows:

$$\begin{cases} p_{n+1} &= p_n - V'(\theta_n) \\ \theta_{n+1} &= \theta_n + p_{n+1} \end{cases} \tag{1.37}$$

In these equations, V' represents the derivative of V with respect to θ. The simplest periodic function for this circular system is the fundamental harmonic function:

$$V(\theta) = -K \sin \theta \tag{1.38}$$

which gives rise to the standard map.

Figure 1.13 illustrates the transition from integrable (regular) dynamics to chaotic dynamics as the parameter K increases. When $K = 0$, the map exhibits integrable behavior and effectively represents a stroboscopic map of a freely rotating particle. This includes both rational and irrational tori, depending on the relationship between the rotation frequency and the strobe frequency. As the kicking strength is increased from zero, while maintaining the same strobe frequency, the irrational tori survive minor perturbations, following the principles of the KAM theorem. Meanwhile, the rational tori

give rise to pairs of stable and unstable orbits as dictated by the Poincaré-Birkhoff theorem. With increasing K, the phase space becomes a mixture of stable and chaotic orbits. At approximately $K \approx 1$, the last remaining rotational irrational KAM tori disintegrates, leading to global diffusion. A stable fixed point endures up to $K = 4$. Beyond $K \approx 5$, the standard map is considered to be chaotic, although it is not conclusively proven to be completely chaotic for any given K value. For an infinite range of K values, stable fixed points are known to emerge on the $p = 0$ line for the torus map, representing accelerator modes for the cylinder map. These modes generally occupy regions of phase space whose areas scale inversely with $1/K^2$. The Lyapunov exponent increases logarithmically as $\ln(K/2)$, providing a very accurate approximation for large K values.

The quantum kicked rotor

The standard map is quantized using the one-period propagator $\hat{U}$, also called the Floquet operator, which evolves the wavefunction of the rotor from one kick to just before the next kick:

$$\phi(\theta; t = n + 1) = \hat{U}\phi(\theta; t = n). \tag{1.39}$$

where the Floquet operator can be written as a product of a δ-kick and a free evolution

$$\hat{U} = \hat{U}_{\text{free}}\,\hat{U}_{\text{kick}} = e^{-i\frac{p^2}{2\hbar}}\, e^{i\frac{K\sin\theta}{\hbar}} \tag{1.40}$$

Here, $\hat{U}$ is the quantum analog of the classical map in Equation (1.37). The parameter K represents the kicking strength. The angular momentum gets quantized to discrete values and provides a complete basis for representing the kicked rotor. Any initial state can be propagated to any desired time by the repeated pre-multiplication by $\hat{U}$.

The unitary time evolution operator $\hat{U}$ has eigenvalues that lie on the unit circle in the complex plane and can be expressed as $e^{-i\epsilon_k/\hbar}$. The phases ϵ_k are called the *quasienergies* as they are similar to the eigenvalues of a quantum Hamiltonian. Similarly, we also have time periodic eigenstates ϕ_k corresponding to each quasienergy, called the Floquet modes [103].

The eigenbasis of the Floquet operator forms a natural basis for representing any initial state, just like the eigenbasis of the Hamiltonian for a static system. In the Floquet basis, the evolution of the state can be trivially written down as

$$|\psi(t)\rangle = \sum_n \langle\psi(0)|\phi_n(0)\rangle\, |\phi_n(t)\rangle\, e^{-i\epsilon_n t/\hbar} \tag{1.41}$$

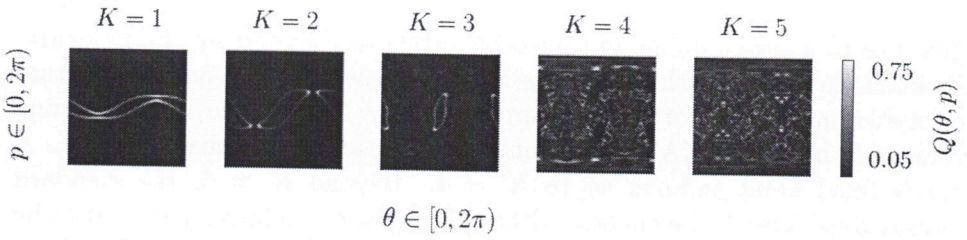

Figure 1.14: Husimi functions of eigenstates of the Floquet operator of the quantum kicked rotor.

One way to visualize the Floquet states in phase space is the Husimi function $Q(\theta, p)$, which associates each phase space point (θ, p) to the value of the overlap between the wavefunction and a wave packet centered at position θ and with mean momentum p. Figure 1.14 shows such Husimi functions for various values of the kicking strength K. The classical phase space structures, as displayed in Figure 1.13, have qualitative similarities to the quantum Floquet eigenstates. In the integrable limit or at very weak chaos, the eigenstate Husimi functions are concentrated on invariant structures of the classical system. In the opposite limit of full-blown chaos, eigenstate Husimi functions are distributed over the whole phase space, reminiscent of the ergodic exploration of phase space of chaotic trajectories. More complicated quantum structures emerge in the intermediate regime of mixed dynamics, for which classically chaos and regularity coexist, more complicated quantum structures emerge.

This correspondence between the eigenstates and classical dynamics can be probed further. One natural path is to investigate the statistical properties of the eigenvalues and eigenfunctions—of time-static Hamiltonians or of the Floquet operator for time-periodic Hamiltonians. Indeed, such statistics provide valuable information about the dynamics of the corresponding classical system. The answers to such questions belong to the subject of random matrix theory, which is introduced in a subsequent section.

Classical emergence

The similarities between classical and quantum phase spaces can be appreciated from a comparison between the phase space structures of Figure 1.13 and the Husimi representation of quantum Floquet eigenstates displayed in Figure 1.14 for the kicked rotor. The transition to chaos is also accompanied by qualitatively different behavior in both cases.

Due to the correspondence principle, classical dynamics must emerge from the quantum map of the kicked rotor as $\hbar \to 0$. However, due to the difference

in the way the states are represented in classical and quantum mechanics, there is no unambiguous way of checking for this correspondence and multiple methods exist. The dynamics of minimum uncertainty wavepacket dynamics is one such method. For small values of $\hbar$, the mean position and momenta of all wavepackets approximately trace out the classical trajectories, for a short time known as the Ehrenfest time, before spreading out and eventually interfering with itself. Furthermore, in the limit $\hbar \to 0$, this correspondence gets better and persists for a longer time scale, and the Ehrenfest time scales logarithmically with $\hbar^{-1}$ for chaotic systems.

The validity of the correspondence principle beyond the Ehrenfest time scale has to be probed in subtler ways. The dynamics of the systems at much later times is encoded in the properties of the eigenvalues and eigenfunctions of the system. Hence, these are the quantities in which one is often most interested.

Superficially it might seem as though the eigenvalues and eigenfunctions have little relation to the classical dynamics in the $\hbar \to 0$ limit. However, this is not true as we saw for the Floquet states for the kicked rotor. Beyond the obvious visual similarities between the classical phase space and Husimi functions of the Floquet eigenstates, more generalized connections exist for the eigenvalues and eigenfunctions, in terms of statistical properties and otherwise. This implies, in particular, that information about the classical chaotic structures, including the rather complex homoclinic and heteroclinic tangles uncovered by Poincaré, must somehow be mysteriously embedded in the eigenproperties as well.

1.2.5 Semiclassical description of chaotic systems

The connection between a quantum system and its classical counterpart is rooted in the classical limit as $\hbar$ approaches zero. This limit is nontrivial and requires formalism. This section provides a brief overview of semiclassical tools for small $\hbar$. We begin with the Bohr-Sommerfeld quantization rule applicable to integrable systems and then explore modern tools for other dynamical regimes.

Bohr-Sommerfeld quantization rule

Consider a one-degree-of-freedom quantum system described by the Hamiltonian operator $\hat{H}_{\text{qu}} = -\frac{\hbar^2}{2m}\frac{d^2}{d\hat{x}^2} + V(\hat{x})$, with a classical analog $H_{\text{cl}}(x,p) = \frac{p^2}{2m} + V(x)$. As the system's Hamiltonian doesn't explicitly depend on time, the total energy of the classical system remains constant. The phase space trajectories are confined to curves $H(x,p) = E$, where E is the initial energy.

The integral

$$J(E) = \oint p\, dx \tag{1.42}$$

along these curves has dimensions of action, equivalent to Planck's constant, $2\pi\hbar$.

The semiclassical regime can be defined by the condition $J(E) \approx \hbar$. In this limit, it can be approximated that the eigenenergies E_n of $\hat{H}_{\text{qu}}$ satisfy the condition

$$J(E_n) = 2\pi\hbar \left(n + \frac{1}{2}\right) \text{ for } n = 0, 1, 2, \ldots \tag{1.43}$$

For systems with more than one degree of freedom, a generalization of this approximation can be obtained for integrable systems. In such cases, classical trajectories in phase space are confined to d-dimensional torus-like manifolds, allowing the definition of action integrals for each path, leading to d quantization conditions, similar to Eq. 1.43, associated with d quantum numbers $n_1, n_2, \ldots, n_d$. This generalization for systems with $d > 1$ degrees of freedom, valid for integrable systems, is known as the Einstein-Brillouin-Keller (EBK) quantization rule.

Gutzwiller trace formula

The Bohr-Sommerfeld quantization rule and its extension to systems with multiple degrees of freedom provide a comprehensive description of the eigenlevels E_n and eigenfunctions $\phi_n(r)$ for quantum systems with integrable classical counterparts. However, this semiclassical approach is limited to systems exhibiting invariant tori in their classical phase space, making it unsuitable for other types of dynamics. An alternative approach, semiclassical trace formulas, offers a solution to analyze quantum spectral properties across various dynamical regimes, including integrable, nearly integrable, fully chaotic, and mixed phase-space systems.

In the fully chaotic regime, we have the Gutzwiller trace formula [104]. The spectrum of $\hat{H}_{\text{qu}}$, comprising energies $E_1, E_2, \ldots$, can be expressed in terms of the density of states function:

$$d(E) = \sum_n \delta(E - E_n) \tag{1.44}$$

Quantum mechanically, $d(E)$ can be represented in terms of the trace of the Green function $G(E)$, giving the approximation its name. Typically, $d(E)$

can be split into two components: a smooth secular part, $d_W(E)$, associated with the classical system's energy surface phase space volume, and the oscillating term, $d_{\text{osc}}(E)$, accounting for quantum fluctuations.

A semiclassical trace formula connects the purely quantum quantity $d_{\text{osc}}(E)$ to a classical counterpart, which is a sum over all periodic orbits j in classical motion. For chaotic classical dynamics, the Gutzwiller trace formula is given by:

$$d_{\text{osc}}(E) = \frac{1}{\pi\hbar}\sum_j \frac{1}{\sqrt{\det(\mathbf{M}_j - 1)}} \cos\left(\frac{1}{\hbar}S_j - \nu_j\frac{\pi}{2}\right). \tag{1.45}$$

Here, S_j is the action integral along orbit j, M_j is the monodromy matrix describing orbit stability, and ν_j is the Maslov index, an integer related to winding around the orbit.

The Gutzwiller trace formula, Eq. 1.45, is applicable in the semiclassical regime and establishes a strong connection between quantum systems and their classical counterparts. This link is evident even in chaotic dynamics, where the Bohr-Sommerfeld-style quantization rule is not applicable. This connection implies that classical dynamics, particularly its chaotic or regular nature, influences purely quantum properties of the system. In Section spectralstatistics, we explore how this relationship manifests for statistical quantities related to the quantum spectrum and eigenfunctions.

Orbit proliferation and convergence issue

The right-hand side of the Gutzwiller trace formula, Eq. 1.45, represents the classical summation over periodic trajectories and is divergent, requiring careful definition due to the creation of delta functions. This divergence is linked to the exponential proliferation of periodic orbits in chaotic systems, quantified by the Lyapunov exponent λ, which measures the rate of divergence of nearby trajectories. The monodromy matrix describes how a perturbation from a periodic orbit evolves over one time period of the orbit. The monodromy matrix of a trajectory j satisfies $\det(M_j - 1) \sim \exp(\lambda\tau_j)$, where τ_j is the period of orbit j. Simultaneously, λ governs the total number of orbits with period τ_j less than some value τ, increasing as $\tau^{-1}\exp(\lambda\tau)$. The exponential growth of terms with rapidly decreasing magnitude persists.

To address the lack of convergence in the classical sum, one approach is to locally smoothen the quantum density of states. This involves replacing the Dirac peaks $\delta(E - E_n)$ in Eq. 1.44 with a function $\delta\epsilon(E - E_n)$ having a finite width ϵ (while maintaining integral unity). A simple method is to introduce a small imaginary part ϵ to the energy ($E \to E + i\epsilon$), yielding a Lorentzian function $\delta\epsilon(E - E_n) = (\pi)^{-1}\epsilon/[(E - E_n)^2 + \epsilon^2]$.

Local smoothing of the quantum spectrum finds various applications. For instance, it can simplify the spectrum when experimental accessibility to fine details is limited, such as when the system interacts with its environment, introducing finite coherence times and broadening energy levels. Another source of smoothing arises from finite temperature, leading to energy-scale averaging on the order of $k_B T$. In some scenarios, the probing scale for the quantum spectrum may be substantially larger than the mean level spacing Δ (i.e., the average energy spacing between successive energy levels). This approach has proven valuable in studying thermodynamic properties of micron-sized quantum dots in GaAs/AlGaAs heterostructures, where the mean level spacing is small compared to the temperature range of interest. In such cases, the Gutzwiller trace formula (or its analog in other dynamical regimes) offers precise predictions and an intuitive interpretation based on a limited set of classical periodic orbits.

Breaking the mean level spacing scale

Describing the fine structure of a quantum spectrum in a semiclassical manner presents challenges. To resolve the mean level spacing (Δ) in a system with d degrees of freedom, very long orbits with periods (τ_j) exceeding the Heisenberg time ($t_H = \frac{\hbar}{\Delta} \sim \hbar^{d-1} \to 0 \to \infty$) must be included in the semiclassical sum. The number of such orbits grows exponentially.

To address these issues, it is crucial to determine if the semiclassical approximation remains valid for such long orbits. Since the limits $\hbar \to 0$ and $t \to \infty$ do not necessarily commute, and a critical timescale t^* for each $\hbar$ exists beyond which semiclassical approximations may fail. It was initially suggested that t^* might correspond to the Ehrenfest time (t_E), related to wave-packet spreading. While t_E exhibits logarithmic dependence, suggesting a shorter timescale, studies showed that semiclassical propagation could exceed t_E. The concept of "long-term accuracy" emerged, indicating that diffraction effects might prevent reaching the Heisenberg time in deep semiclassical limits.

Even if t* is larger than t_H, the proliferation of orbits poses a challenge. The semiclassical sum in the Gutzwiller formula is divergent, requiring significant cancellations between terms. Understanding these cancellations and the structure of classical periodic orbits becomes essential. Mathematical objects with less singular behavior, such as spectral determinants, were introduced to address this issue. Semiclassical expansions for these objects exhibit less divergence. Techniques like dynamical zeta functions and cycle expansions were also introduced to express the quantum spectrum in alternative ways.

An improved understanding of long periodic orbits has helped enhance

the convergence properties of semiclassical periodic orbit expansions. The "cycle expansion" method, which decomposes longer orbits into shorter ones and regroups terms, has improved convergence properties.

In summary, semiclassical trace formulas establish a connection between quantum and classical systems by expressing quantum energy spectra in terms of classical periodic orbits. Short orbits provide a simple interpretation of quantum behavior while resolving finer spectral details involves considering much longer orbits and employing sophisticated techniques like spectral determinants, dynamical zeta functions, and cycle expansions.

1.2.6 Random Matrix Theory

In the previous section, we discussed the existence of semiclassical approximations like the Gutzwiller trace formula, which establishes a connection between quantum and classical systems. This suggests that the qualitative nature of classical dynamics influences quantum properties. While Einstein-Brillioun-Keller quantization hinted at this influence on eigenstates, it couldn't predict eigenstates for chaotic systems. The goal is to understand these properties quantitatively, a subject known as spectral statistics.

One crucial tool for this purpose is random matrix theory. It was initially introduced by Wigner to explain the spectral statistics of strongly interacting many-body systems, like heavy nuclei, long before the dynamical distinctions and Gutzwiller trace formula were understood. Since then, the role of chaos and the connection between trace formulae and random matrix theories have become evident. A remarkable example of this connection between seemingly unrelated concepts—chaotic trajectories and random matrices—has emerged from the study of spectral statistics. As mentioned in the introduction, random matrix theory implies universality in statistical properties, meaning that much system-specific information vanishes from these properties. Surprisingly, even though chaotic systems have unique trajectories, these trajectories when considered in terms of their quantum counterparts and weighted by their instabilities, uniformly explore their respective phase spaces. This uniformity results in a loss of information, leading to universal features in widely different systems which can be captured by random matrix theory.

Spectral statistics

avoid beginning a sentence with a symbol

For any quantum system having a classical limit, three distinct energy scales can be defined. δE^{cl}, is the scale at which classical dynamics changes appreciably. This energy scale is independent of Planck's constant, i.e., $\delta E^{\mathrm{cl}} \sim \hbar^0$. The Thouless energy $E^{\mathrm{Th}} = \hbar/t_{\mathrm{fl}} \sim \hbar^1$, where the "time of flight" t_{fl} is the

is

typical classical time to diffuse through the system. And the mean energy level spacing Δ, which scales as $\sim \hbar^d$ where d as the number of degrees of freedom).

In the semiclassical limit $\hbar \to 0$, with two or more degrees of freedom, there is a separation between these energy scales. Within an energy range smaller than $\delta E^{\rm cl}$, where classical dynamics remains constant, there may be a very large number of Thouless energy slices, each, in turn, containing a very large number of discrete energy levels. Energy levels in different Thouless slices are essentially independent and the expected value of any spectral quantity $\langle f(\{E_i\})\rangle$ can be taken to be the statistical mean over various such slices.

One fundamental quantity that can be defined in this manner is the mean density of states $\langle\hat{\rho}(E)\rangle$, which counts the average number of energy levels in a specified energy interval. The local mean level spacing Δ is the inverse of $\langle\hat{\rho}(E)\rangle$. $\langle\hat{\rho}(E)\rangle$ is primarily determined by the volume of the classical energy surface $H^{\rm cl}(r,p) = E$ and is independent of the character of the classical motion. Correlations between energy levels are usually studied by transforming the original eigenenergies $\{E_1, E_2, E_3, \ldots\}$ into a rescaled sequence $\{x_1, x_2, x_3, \ldots\}$ with the same fluctuations properties but a mean density of one.

Several relevant quantities have been constructed to measure the fluctuation properties of $\{x_i\}$. The number of rescaled levels x_i in an interval of length r near an energy E, is denoted by $N_E(r)$. By construction, $\langle N_E(r)\rangle \sim r$ since the average density of x_i is one. However, $\Sigma^2(r)$, which measures the variance of $N_E(r)$, contains valuable information about the fluctuation properties of the spectrum. It provides insights into how likely levels are to cluster at short ranges (for small r) and how elastic or rigid the spectrum is at large ranges. Another important quantity is the nearest neighbor density $P(s)$, which measures the probability of two successive rescaled levels x_i and x_{i+1} being separated by a distance s.

For a Poisson sequence of energies where the $\{x_i\}$ are independent numbers randomly taken with a mean density of one,

$$P_{\rm Poisson}(s) = \exp(-s), \tag{1.46}$$

$$\Sigma^2_{\rm Poisson}(r) = r. \tag{1.47}$$

Poisson statistics represent the extreme case of no correlation. Comparing these statistics with those derived from a specific spectrum provides a quantitative assessment of the amount of correlations present.

Random Matrix Ensembles

Random matrix ensembles were introduced into physics by Wigner in the 1950s to describe the statistical properties of slow neutron resonances, which correspond to highly excited states of nuclei. Due to the complexity of nuclear systems, it was deemed unfeasible and unhelpful to individually evaluate these energy levels. Instead, Wigner suggested describing their statistical properties using random matrices.

Quantum Hamiltonians, whether for nuclei or simpler systems like the Hydrogen atom, can be represented as matrices because they act as linear operators on the space of wavefunctions. To make the modeling manageable, a finite $N \times N$ matrix is used to represent the neighborhood of a given energy E. Wigner's idea was that, due to the complexity of nuclear dynamics, the experimentally obtained spectral statistics of neutron resonances match with random matrix elements.

However, the random matrices are constrained by the symmetries of the physical systems. The matrix representing a quantum Hamiltonian must be Hermitian. For example, Hamiltonians for nuclei are invariant under rotations of physical space, and they should be analyzed with fixed values of relevant quantum numbers that arise from system symmetries. Time reversal invariant Hamiltonians, for systems without spin, are represented by real symmetric matrices.

Wigner introduced three random matrix ensembles to account for these symmetry constraints: the Gaussian Unitary Ensemble (GUE) for systems with broken time reversal invariance, and the Gaussian Orthogonal Ensemble (GOE) for systems with preserved time reversal invariance and no spin degrees of freedom. These ensembles serve to model the spectral statistics of these complex systems.

Spectral statistics, such as the nearest neighbor distribution $P(s)$ and the variance $\Sigma^2(r)$, have been computed for these ensembles. The distributions for $P(s)$ in the GOE and GUE cases are characterized by strong level repulsion, meaning that zero-distance spacings are avoided, and for small spacings, the probability of occurrence is low compared to uncorrelated spectra. The statistics for $\Sigma^2(r)$ in random matrix ensembles exhibit level rigidity, with fluctuations around the mean value significantly smaller than in Poissonian statistics, even for long sequences.

Here are expressions for $P(s)$ in the random matrix ensembles:

$$P_{\text{GOE}}(s) = \frac{\pi}{2} s e^{-\frac{\pi s^2}{4}} \quad \text{(GOE)}, \tag{1.48}$$

$$P_{\text{GUE}}(s) = \frac{32}{\pi^2} s^2 e^{-\frac{4s^2}{\pi}} \quad \text{(GUE)}. \tag{1.49}$$

Additionally, the asymptotic expression for $\Sigma^2(r)$ in the GOE case as r becomes large is given by:

$$\Sigma^2_{\text{RMT}}(r) \approx \frac{2}{\pi^2} \ln(r) \quad (r \gg 1) \tag{1.50}$$

This result illustrates the strong level rigidity in random matrix statistics.

Quantum chaos and Random matrices

Random matrix ensembles, like GOE or GUE, offer random representations of model Hamiltonians, allowing the evaluation and comparison of spectral statistics such as the nearest neighbor distribution $P(s)$ and $\Sigma^2(r)$ statistics with other models or experimental data. When applied to nuclear resonances, random matrix theory (RMT) predictions have shown strong agreement with actual nuclear spectral statistics.

Bohigas, Giannoni, and Schmit proposed in 1984 that even "simple" systems could exhibit statistical behavior similar to RMT [105]. They demonstrated this with numerical analysis of two-dimensional billiards, such as the stadium billiard, which displayed RMT-like statistics. These systems, while not complex, are chaotic despite having only two degrees of freedom and a simple Hamiltonian.

This led to the conjecture that "simple" systems could exhibit RMT-like spectral fluctuations if their classical analog dynamics were chaotic. The role of complexity in nuclear systems is seen as providing chaotic dynamics rather than being inherently complex, as originally suggested by Wigner. Although there isn't a complete formal proof of the Bohigas, Giannoni, and Schmit (BGS) conjecture, it is strongly supported by semiclassical theory. The connection between semiclassical trace formulae and random matrices has been established through the uniformity principle of periodic orbits in chaotic systems.

Berry and Tabor [106] showed that generic integrable systems exhibit spectral statistics closer to the Poissonian case, lacking level repulsion and rigidity. Mixed dynamics, where chaos and regularity coexist, is more complex and requires the implementation of non-universal time scales, leading to transition matrix ensembles with non-universal characteristics.

Analyzing the kicked rotor suggests that the near-integrable regime displays Poisson-like statistics, while the strongly chaotic regime exhibits RMT-like statistics. This observation aligns with the comparison of sample Poisson and random matrix spectra. Further calculations confirm excellent agreement with the expressions provided.

Random matrix theory and quantum chaos are connected to important mathematical relations, including the Riemann zeta function and the Riemann hypothesis. The statistical properties of the imaginary components of the non-trivial zeros of the Riemann zeta function match those of the GUE, and there is an analogous Selberg trace formula, exact for the Riemann zeta function. Consequently, the Riemann zeta function serves as a mathematically rigorous platform for the study of quantum chaos.

1.2.7 The quantum measurement problem

The collapse of the wavefunction is probably the biggest chink in the glorious armor of quantum mechanics. While every quantum system evolves in a unitary, deterministic fashion following the Schrödinger equation, the process of measurement is somehow exempt from this rule. Although this poses no problems for the practicing physicist, the unsatisfactory state of affairs has been echoed time and again by all who have given it any serious thought [107–111].

Despite long-standing efforts, there is no universally accepted solution to the measurement problem. Most approaches can be broadly classified into one of two buckets.

Epistemic approaches place the focus on knowledge and experiences. They suggest that the wavefunction doesn't represent the physical reality itself but is merely a tool for tracking what agents know about it. Interpretations like the Copenhagen interpretation and QBism adhere to this view.

On the other hand, in the *ontic* approaches, the wavefunction is proposed to completely and precisely describe reality. It contends that measurements do not collapse the wavefunction but result in entanglement. The many-worlds interpretation is a well-known example of this stance.

Below we briefly outline some of the more popular approaches.

The Copenhagen interpretation

> Observations not only disturb what is to be measured, they produce it.
>
> PASCUAL JORDAN [112]

Historically, the measurement problem can be traced back to Niels Bohr's "Copenhagen interpretation", where he proposed that the physical properties of quantum systems depend on experimental conditions, including measurements. Bohr suggested that measurement is a fundamental aspect of defining

physical quantities in quantum systems. However, his interpretation did not view this dependence as causal but rather as a relational concept, akin to the relative nature of space and time in special relativity. These among other views led to the famous Bohr-Einstein debates [113], where Einstein took a realist position, contending that measurements reflect an independently existing reality. He argued that if a physical quantity could be predicted with certainty without disturbing a system, then there exists an element of physical reality corresponding to that quantity. In this realist perspective, observations merely passively reflect what is independently real.

The Copenhagen interpretation posits that, whenever an observation is made, the wavefunction of a quantum system collapses instantly to an eigenstate of the observable being measured. Many questions have been raised [114] regarding what constitutes an observation. "But laws of nature differing from the usual ones cannot apply during a measurement," Schrödinger writes in [107] (translated in [115]), "for objectively viewed it is a natural process like any other, and it cannot interrupt the orderly course of natural events." This departure from the deterministic unitary evolution during measurement, leading to a definite outcome later came to be called the 'measurement problem'. "It would seem that the theory is exclusively concerned about 'results of measurement', and has nothing to say about anything else" wrote John Bell [108]. These objections have remained largely unanswered, and are considered to belong to the domain of philosophy rather than physics.

In a review paper, Bassi *et al.* [116] write "The Copenhagen interpretation (Bohr, 1928) [reprinted in Wheeler and Zurek (1983)] postulates an artificial divide between the microworld and the macroworld, without quantitatively specifying at what mass scale the divide should be. Microscopic objects obey the rules of quantum theory (superposition holds) and macroscopic objects obey the rules of classical mechanics (superposition does not hold). During a measurement, when a microsystem interacts with a macrosystem, the wave function of the microsystem "collapses" from being in a superposition of the eigenstates of the measured observable to being in just one of the eigenstates". The Copenhagen interpretation gives no definite answer to why and where this 'shifty split' between the classical and the quantum is to be placed. Worse yet, it provides no rationale as to why a measurement does not follow the Schrödinger equation. In Chapter 4 we investigate the consequences of such a split. Wigner and von Neumann implicated conscious observation as the cause of wavefunction collapse. von Neumann found that lifting the split between the classical and quantum worlds led to entanglement between the system and measurement apparatus. If we assume that the system and

apparatus have states $|\psi_S\rangle$ and $|\psi_A\rangle$ before the measurement,

$$|\psi_S\rangle\,|\psi_A\rangle \xrightarrow{\text{measurement}} \sum_n c_n\,|\phi_S^n\rangle\,|\psi_A^n\rangle. \tag{1.51}$$

Bell has echoed the discomfiture of bringing consciousness into fundamental theory best—"What exactly qualifies some physical systems to play the role of 'measurer'?" [108] he asks. Could the wavefunction of the universe have been waiting for all this time for a conscious being to measure it so it could finally collapse? He admonishes the use of such vague notions as 'measurement' and 'observer' in a fundamental theory of the universe.

1.2.8 Decoherence

> ... a normal consequence of interacting quantum mechanical systems. It can hardly be denied to occur—but it cannot explain anything that could not have been explained before. Remarkable is only its quantitative (realistic) aspect that seems to have been overlooked for long.
>
> HEINZ-DIETER ZEH [117]

As desirable as it may be to study and experiment on isolated systems, no system can be truly isolated. Microscopic quantum systems inevitably interact and get entangled with the environmental degrees of freedom, which are outside our ability to directly measure or control [118]. Hence the effect of this entanglement can only be treated in a statistical sense. In essence, we average the state of the system over all possible realizations of the environment, by taking a partial trace over the environment degrees of freedom of the system-environment density operator. This has the effect of decaying the off-diagonal terms in the reduced system density matrix, which suppresses interference effects and hence the process is called *decoherence*. This process has a very short time scale and can occur in the presence of a very minimal environment [119]. It has a big role to play in the appearance of the classical world from quantum laws [120]. It must be stated that decoherence is not an interpretation as it is a direct consequence of the laws of quantum mechanics.

The decoherence program has been able to shed light on two aspects of the quantum measurement problem

1. Definite outcomes in the measurement process can be explained in terms of effective superselection rules imposed by the form of the in-

teraction with the environment. These emergent states are called the pointer states [121–124].

2. The decay of the coherences in the density matrix in these pointer bases explains why interference effects do not manifest at the macroscopic scale, despite being governed by quantum mechanics.

It is also possible to derive Born's rule using some plausible assumptions based on the ideas of decoherence [125–127]. The difficulty of shielding from the environment gives rise to the appearance of irreversibility in the classical limit [128]. Although decoherence is unable to completely solve the quantum measurement problem, it illuminates parts of the puzzle of quantum to classical transition.

1.2.9 Objective collapse theories

These collapse models [116, 129] do not need the intervention of a conscious observer, accomplished by making non-linear and stochastic adjustments to the Schrödinger equation. These modifications introduce the concept of wave function collapse into the standard quantum evolution. These models posit that there is an intrinsic propensity of particles to spontaneously localize. The free parameters of these models are tuned so as to closely approach the quantum mechanical predictions while also explaining the appearance of classical behavior of macroscopic objects [130]. A wide range of collapse models with different localization basis have been developed: [131, 132] and [133] localize in the energy, momentum and spin basis respectively, while the Ghirardi-Rimini-Weber (GRW) [134] and the *Continuous Spontaneous Localisation* (CSL)[135] models localize in the position basis.

The fundamental concept underlying the dynamical reduction program can be summarized as follows: Spontaneous and stochastic wave function collapses occur continuously, affecting all particles, whether they are in isolation or interacting with others, be it in the form of individual atoms or within intricate measuring devices. It is essential that these collapses remain infrequent and subtle when dealing with microscopic systems to preserve their quantum characteristics as dictated by the Schrödinger equation. Simultaneously, these collapses must cumulatively impact the global system when a multitude of particles assemble to create a macroscopic entity. In such cases, numerous collapses, each involving a single particle, influence the macro-system frequently, ultimately compelling the wave function of the macro-system to localize in space.

On a mathematical level, the dynamical reduction program is executed by introducing novel terms into the Schrödinger evolution with specific characteristics:

1. *Nonlinearity*: These new dynamics must break the superposition principle at the macroscopic level, ensuring the localization of the wave function of macroscopic objects.

2. *Stochasticity*: When describing measurement-like scenarios, the dynamics must elucidate why outcomes occur randomly, conforming to the Born probability rule.

3. *Amplification Mechanism*: The introduced terms must have minimal effects on the dynamics of microscopic systems while having a significant impact on large, many-particle systems like macroscopic objects, leading to their classical-like behavior.

4. *Superluminal signaling*: It is vital that the nonlinear terms do not enable superluminal signaling to preserve the causal structure of spacetime. It is prevented by introducing stochasticity.

It is noteworthy that these requirements are highly demanding, and there is no inherent guarantee that they can be consistently met. One of the notable achievements of collapse models is their ability to demonstrate the feasibility of implementing this program in a coherent and satisfactory manner.

Stripped of intricate details, the core dynamics can be expressed through the following stochastic differential equation for the wave function:

$$d\left|\psi_t\right\rangle = \left[-\frac{i}{\hbar}\hat{H}dt + \sqrt{\lambda}\left(\hat{A} - \langle\hat{A}\rangle_t\right)dW_t - \frac{\lambda}{2}\left(\hat{A} - \langle\hat{A}\rangle_t\right)^2 dt\right]\left|\psi_t\right\rangle. \quad (1.52)$$

In this equation, $\hat{H}$ is the quantum Hamiltonian of the system, $\langle\hat{A}\rangle_t$ represents the quantum expectation value of the self-adjoint operator $\hat{A}$ at time t, λ is a positive constant that determines the strength of the collapse mechanism, and W_t is a standard Wiener process.

Equation (1.52) can be conceptually grasped quite easily. It characterizes a diffusion process occurring within the unit sphere of the Hilbert space, ensuring the conservation of the wave function's norm. $\hat{H}$ induces a unitary "rotation" on this sphere, while the remaining terms work in a stochastic manner to collapse the wave function toward one of the eigenstates of the operator $\hat{A}$. The interplay between these terms depends on their relative strength. If the dynamics influenced by $\hat{H}$ predominates, the evolution remains mostly deterministic with only slight blurring by the collapse terms

over extended periods. Conversely, when the collapse terms dominate, the wave function rapidly undergoes random collapses, following a probability distribution nearly matching the Born probability rule.

An interesting point to note is that, though the variations among different collapse models can be substantial, they all share a common structure captured by Equation (1.52). This consistency is not coincidental. It can be demonstrated that the necessity of preserving the principle of no-faster-than-light signaling, coupled with the requirement of norm conservation, essentially dictates the form of possible modifications to the Schrödinger equation. Thus, one could argue that collapse models are not merely one of several possible approaches to modifying quantum theory but are, in a sense, the exclusive path to do so.

Collapse models in position space

The choice of the operator $\hat{A}$ in Equation (1.52) plays a pivotal role in determining the basis in which the wave function localizes. If $\hat{A}$ equals the Hamiltonian ($\hat{A} = \hat{H}$), the collapse takes place in the energy basis, and if $\hat{A}$ corresponds to momentum ($\hat{A} = \hat{p}$), the collapse occurs in the momentum basis, and so forth. Given that the primary motivation for introducing collapse models is to account for the classical behavior of macroscopic objects, notably their well-defined positions in position space, the most straightforward and intuitive choice is to set $\hat{A}$ equal to the position operator $\hat{q}$ or some function of it. All the collapse models found in the literature follow this pattern. The first model of this kind was the GRW (Ghirardi–Rimini–Weber) model [136], defined in terms of a discrete jump process while maintaining dynamic equivalence with Equation (1.52). This concept later evolved into the CSL (Continuous Spontaneous Localisation) model [137], which includes identical particles in its description. Concurrently, the QMUPL (Quantum Mechanics with Universal Position Localisation) model [138] emerged as a short-distance approximation to both the GRW and CSL models [139]. The DP (Diosi–Penrose) model [140] also deserves mention as an initial attempt to connect wave function collapse to gravity.

Qualitatively, these models share a common feature: they induce wave function collapse in space, and the larger the collection of particles in interaction with each other is, the faster the collapse of the macroscopic object. Quantitatively, these models exhibit variations, sometimes substantial. They share another common trait: the noise responsible for the collapse of the wave function also induces Brownian-type motion in the system. In momentum space, the wave function acquires increasingly higher components, resulting in a steady increase in kinetic energy. While this increase is small and hardly

detectable with current technology, it remains an undesirable aspect of these models.

Recently, a partial solution to this issue has been found. It has been demonstrated that it is possible to introduce dissipative effects into collapse models without altering their collapse properties. This achievement has been successful for the QMPUL model [141], the GRW model [136], and the CSL model [142], giving rise to what is termed dissipative models (dQMUPL, dGRW, dCSL). Intriguingly, this approach encountered more challenges in the case of the DP model [143]. In all these instances, energy no longer increases but instead thermalizes to a finite temperature associated with the noise responsible for the collapse. A common misconception used as an argument against these models is that collapsing the wave function in space increases momentum uncertainty, and hence kinetic energy, due to Heisenberg's uncertainty principle. This can lead to nonconservation of energy in the macroscopic limit, something which is not observed in practice. The dissipative modifications to these models not only demonstrate that energy increase is not an inherent feature of collapse models but also that, in fact, energy can decrease if it is initially higher than the noise energy. Dissipative collapse models suggest the following scenario: the noise causing the collapse is a real field filling space, at thermal equilibrium at a certain temperature T, and it nonlinearly couples with quantum systems, causing wave function localization in space while simultaneously thermalizing them to their own temperature. This second effect is akin to how classical particles behave in a thermal environment. Although energy is not conserved in this process, there is a path toward restoring energy conservation by considering the system's reaction to the noise, similar to classical physics where fundamental equations of motion (Newton's laws) lead to energy conservation. However, for collapse models, achieving this requires establishing an underlying theory from which they emerge as phenomenological models—a task that is yet to be completed (see [4] for an initial attempt), but their argument suggests that its feasibility is not unreasonable.

that article is from 1907, how can it be about wave function collapse?

Thus far, all models have been defined with white noise in time, which is a convenient mathematical idealization. Real noises invariably have a frequency cutoff. Colored-noise-based collapse models have been introduced [144–148], demonstrating that they share the same essential properties as the original models, although specific details may differ, particularly in cases with low-frequency cutoffs.

The mass-proportional CSL model

The most extensively studied model in the literature is the mass-proportional version of the CSL model [149]. Its dynamics can be described by the following stochastic differential equation:

$$\begin{aligned} d\left|\psi_t\right\rangle \;=\; & \left[-\frac{i}{\hbar}\hat{H}dt+\frac{\sqrt{\gamma}}{m_0}\int d^3x\left(\hat{M}(x)-\langle\hat{M}(x)\rangle_t\right)dW_t(x)\right. \\ & -\frac{\gamma}{2m_0^2}\iint d^3xd^3yG(x-y)(\hat{M}(x) \\ & \left.-\langle\hat{M}(x)\rangle_t)(\hat{M}(y)-\langle\hat{M}(y)\rangle_t)\right]\left|\psi_t\right\rangle \end{aligned} \tag{1.53}$$

In this equation, γ (with dimensions of $[L^3T^{-1}]$) represents the model's collapse strength, m_0 is a reference mass, typically set to the mass of a nucleon, and $\hat{M}(x)=m\hat{a}^\dagger(x)\hat{a}(x)$ is the mass density operator, where $\hat{a}^\dagger(x)$ and $\hat{a}(x)$ are the creation and annihilation operators for a particle at point x in space (spin is ignored in this context). These operators serve as a suitable replacement for the position operator in the second-quantized language. $W_t(x)$ is a family of Wiener processes, each associated with a specific spatial point and characterized by an average of zero. These processes are "white" in time but exhibit a Gaussian correlation function in space, given by

$$E\left[W_t(x)W_s(y)\right]=\delta(t-s)G(x-y),$$

$$G(x-y)=\frac{1}{(4\pi r_C)^{3/2}}\exp\left[-(x)^2/4r_C^2\right].$$

why are these equations unnumbered?

no γ dependence?

The CSL model relies on two key phenomenological parameters: the collapse strength γ and the correlation length of the noise, r_C. Typically, γ is substituted with $\lambda=\gamma/(4\pi r_C^2)^{3/2}$, which has the dimensions of a rate $[\mathrm{T}^{-1}]$. Experimental analysis continually imposes increasingly stringent constraints on these parameters.

The amplification mechanism

The CSL equation (1.53) shares the common objective of wave function localization in space, its effectiveness determined by the relative strength in comparison to the Hamiltonian $\hat{H}$. To delve deeper into how the collapse terms operate, consider a system, particularly a rigid object, where the center of mass exists in a state that spans a distance Δx much smaller than r_C. In such cases, it can be demonstrated that the collapse is nearly negligible. Essentially, the degree of delocalization is too minuscule, and the noise,

capable of resolving only distances greater than r_C, already perceives it as well-localized. However, if the extent of delocalization exceeds r_C, the noise compels the wave function to collapse at a rate roughly approximated by:

$$\Lambda = \lambda n^2 N. \tag{1.54}$$

Here, γ, as mentioned earlier, represents the collapse rate for a single nucleon, n quantifies the number of nucleons within a volume of r_C^3 (reflecting the density of matter), and N counts how many such volumes can fit within the space occupied by the system (indicating the total size of the system). Equation (1.54) encapsulates the mathematical expression of the amplification mechanism: the larger the system, the swifter the collapse. This means it is possible to select a specific combination of values for γ and r_C in such a way that, at the microscopic level, CSL closely resembles standard quantum mechanics. Simultaneously, at the macroscopic level, it compels wave functions to be tightly localized in space. Consequently, the model offers a unified framework for describing both the quantum properties of macroscopic systems and the classical characteristics of macroscopic objects. It notably addresses the quantum measurement problem. In the literature, two sets of CSL parameters have been proposed. The initial proposal advocated for $\lambda \equiv 10^{-17}$ s^{-1} and $r_C = 10^{-7}$ m. More recently, Adler has suggested significantly enhanced values for λ, driven by the necessity to make wave function collapse effective at the latent image formation level in photographic processes. The values proposed by Adler are approximately $10^{9\pm2}$ times larger than the standard values for $r_C = 10^{-7}$ m and roughly $10^{11\pm2}$ times larger for $r_C = 10^{-6}$ m [150].

I think you want to refer to λ, not γ

I don't understand this.

Experimental tests

Collapse models introduce explicit modifications to the Schrödinger equation, leading to predictions that, in most cases, deviate slightly from those of standard quantum mechanics and are subject to experimental verification. Two categories of tests, interferometric and non-interferometric, are employed to evaluate these models.

Interferometric experiments represent the most direct approach to assess collapse models. Given that their primary objective is to preclude the existence of macroscopic superpositions, the logical approach is to take a macroscopic object, prepare it in a superposition of eigenstates, maintain it for an extended duration, and then observe the presence of quantum interference. Objective collapse models predict no interference, contrary to the expectations of ordinary quantum mechanics. However, conducting such experiments is exceedingly challenging due to various technical hurdles. A

notable achievement by Markus Arndt's group in Vienna involved superimposing and detecting quantum interference of the center of mass of a macromolecule with a mass of 20,000 atomic mass units (a.m.u.), currently a world record [151]. Notably, neither Adler's values for λ and r_C nor those of GRW are refuted by this experiment, indicating that the mass involved, the superposition times, and distances are sufficiently substantial. Optomechanics holds the promise to advance beyond the current state of the art [152], although it requires technological improvements.

Non-interferometric tests [153–156] aim to measure the Brownian motion induced by the noise, independent of the collapse phenomenon. Two effects have been investigated in particular. The first is the increase in kinetic energy. A system confined in a harmonic trap should exhibit more pronounced tremors around the equilibrium position than predicted by quantum mechanics. A recent experiment [157] involving a cantilever was able to set a strong constraint, partially excluding Adler's value for λ. The second effect involves the spontaneous emission of radiation from charged particles due to acceleration induced by the noise. Experimental data [158] in the X-ray region have been gathered, which also exclude Adler's value for λ. Future experiments hold the potential to establish bounds at least two orders of magnitude stronger.

It is worth noting that interferometric bounds derived from matter-wave interferometry are robust against alterations in the collapse equation, such as the introduction of dissipative effects or changes in the type of noise [159]. As a result, these bounds serve the purpose of testing the entire class of collapse models in space, not limited to a single model like CSL. Conversely, non-interferometric tests are more sensitive to the specific characteristics of the model.

For instance, predictions regarding spontaneous photon emission are highly dependent on the autocorrelation function of the noise. While these bounds are formidable, they may not encompass the entire spectrum of collapse models. A combined approach that incorporates both interferometric and non-interferometric experiments will likely be necessary to comprehensively test collapse models and, consequently, the quantum superposition principle in a meaningful manner. Collapse models offer a coherent framework for understanding the collapse of the wave function as a dynamic process, achieved through suitable adjustments to the Schrödinger equation. While one anticipates that they should ultimately stem from an underlying theory, providing a comprehensive description that accounts for both quantum evolution and wave function collapse in an appropriate coarse-grained manner remains a challenging, unsolved problem. In the interim, it remains intriguing and relevant to subject these models to experimental scrutiny, primarily because

every such experiment essentially tests the fundamental superposition principle, a cornerstone of quantum theory.

Until recently, collapse models primarily resided within the realm of theoretical conjecture. However, there has been a growing surge in experimental endeavors to test them. Advancements in technology have enabled and will continue to enable, the exploration of significant portions of the parameter space. In due course, it will be captivating to observe whether nature imposes limitations on nonlinear modifications to quantum theory or, even more intriguingly, whether the superposition principle itself may encounter its limits.

1.2.10 Bohmian mechanics

Bohm's innovative approach (Bohm, 1952; Bohm and Bub, 1966; Bohm and Hiley, 1993) represents a noteworthy modification of de Broglie's initial "pilot-wave" concept from 1930. In the framework of Bohmian mechanics, a system consisting of N nonrelativistic particles is described by two fundamental components: a wave function $\psi(t)$ and a configuration $\mathcal{Q}(t) = (\mathbf{q}_1(t), \ldots, \mathbf{q}_N(t)) \in \mathbb{R}^{3N}$, which encapsulates the positions of the individual particles $\mathbf{q}_i(t)$. This dual representation, denoted as $(\psi, \mathcal{Q})$ for each moment t, governs the system's state. The dynamics of the system are driven by two distinct equations. The evolution of the wave function $\psi(t)$ follows the standard Schrödinger equation, $i\hbar(\partial/\partial t)\psi = \hat{H}\psi$, while the particle positions $\mathbf{q}_i(t)$ in the configuration $\mathcal{Q}(t)$ are guided by the "guiding equation":

$$\frac{d\mathbf{q}_i}{dt} = \mathbf{v}_i^{\psi}(\mathbf{q}_1, \ldots, \mathbf{q}_N) \equiv \frac{\hbar}{m_i} \operatorname{Im} \frac{\nabla_{q_i}\psi}{\psi},$$

where m_i signifies the mass of the i-th particle. As a result, the particles follow well-defined trajectories as described by $\mathcal{Q}(t)$, and their distribution is shaped by the quantum equilibrium distribution $\rho = |\psi|^2$.

One of the central criticisms leveled against Bohm's theory is its attribution of fundamental ontological status to particles. This view has encountered frequent opposition, as general arguments challenging the fundamental nature of particles within any relativistic quantum theory have been extensively discussed (see, for instance, Malament, 1996, and Halvorson and Clifton, 2002).

1.2.11 Relative-state interpretations

Everett's original proposal [160] for a relative-state interpretation of quantum mechanics has led to various strands of interpretations. Everett's theory

was not explicitly detailed, leading to several interpretations. The standard quantum mechanics system-observer duality introduces external "observers" with stochastic indeterminism, but this raises issues when considering the entire universe, where no external observers exist. Everett's central idea is to abandon duality, assuming the existence of a total state representing the entire universe. This total state upholds the universal validity of the Schrödinger evolution, postulating that all terms in the superposition of the total state after measurement correspond to physical states.

Each of these physical states can be seen as relative to the state of the other part of the composite system, known as "branches" in Everett's original proposal. This concept leads to the many-worlds interpretation and the many-minds interpretation. In other words, each term in the final-state superposition represents an equally "real" physical state of affairs realized in different branches of reality.

Those inclined toward relative-state interpretations, such as decoherence adherents, find compatibility with the Everett approach since it takes unitary quantum mechanics as is, with minimal interpretive elements. On the other hand, proponents of relative-state interpretations have used the mechanism of decoherence to resolve associated difficulties.

Relative-state interpretations come with two core challenges: the preferred-basis problem and the interpretation of probabilities in a framework where every outcome occurs in some world or mind.

1.2.12 Consistent histories

The consistent (or decoherent) histories approach was introduced by Griffiths [161–163] and further developed by Omnès [164–170], Gell-Mann and Hartle [171–174], Dowker and Halliwell [175], and others. Reviews of the program can be found in the papers by Omnès [168] and Halliwell [176, 177]; thoughtful critiques investigating key features and assumptions of the approach have been given, for example, by d'Espagnat [178], Dowker and Kent [179, 180], Kent [181], and Bassi and Ghirardi [182].

In essence, the consistent-histories method aims to remove the central importance of measurements in quantum mechanics. Instead, it focuses on examining quantum histories, which are sequences of events depicted by sets of projection operators ordered in time, and assigning probabilities to these histories. Initially inspired by quantum cosmology, which explores the evolution of the entire universe as a closed system, this interpretation removes the role of the external observer, unlike the Copenhagen interpretation, which considers them essential.

The consistent-histories interpretation assigns probabilities to alternate

sets of histories in a way that is consistent with the rules of classical probability theory while simultaneously obeying the Schrödinger equation. Omnés writes in [183] that the consistent-histories framework is capable of justifying why a certain set of classical questions can or cannot be asked of a quantum system and can help us understand the limits of classical logic when applied to quantum systems.

1.2.13 Generalized quantum measurements

The operational approach to quantum mechanics [184–186] has, among other things, systematically expanded the notion of ideal projective measurements to include imprecise and unsharp measurements. This has been fruitful for several practical [187–189] as well as foundational problems [190, 191].

Unsharp measurements have been used to maintain coherence in the presence of noise [187]. Choudhary *et al.* [188] have suggested their application in the measurement of qubit levels of a trapped ion. The evolution of a superconducting qubit subjected to unsharp measurement has been investigated [189]. Schemes for reliable state estimation with sequential [192] and continuous-time unsharp measurements [193] have been suggested.

A special class of quantum measurements, called quantum non-demolition (QND) measurements have been widely used in monitoring a quantum oscillator [194, 195]. This form of measurement can in principle leave the quantum state undisturbed. This could be useful for extremely high precision measurements such as in certain schemes of gravitational wave detection. The statistical behavior of a quantum oscillator subjected to a sequence of QND measurements has been formally worked out by Matta and Pierro [196].

Textbook quantum mechanics exposes us to an idealized measurement where the state collapses to an eigenstate of the measured observable. Such a measurement, called von Neumann measurement, is described by projection-valued measures (PVM). This is framed in terms of a set of projection operators $\{\widehat{P}_i\}$ where the index i runs over all possible measurement outcomes for the observable of interest. These have the following properties [197]

Hermiticity	$\widehat{P}_i = \widehat{P}_i^\dagger$
Positive-semidefiniteness	$\widehat{P}_i \geq 0$
Idempotence	$\widehat{P}_i^2 = \widehat{P}_i$
Orthogonality	$\widehat{P}_i \widehat{P}_j = \delta_{ij}$
Resolution of identity	$\Sigma_i \widehat{P}_i = \mathbb{I}$

The probability of obtaining outcome i when measuring a state $|\psi\rangle$ is

given by

$$p(i|\psi) = \langle\psi|\,\widehat{P}_i\,|\psi\rangle \tag{1.55}$$

and the post-measurement state becomes

$$|\psi_{\text{post}}\rangle = \frac{\widehat{P}_i\,|\psi\rangle}{\sqrt{\langle\psi|\,\widehat{P}_i\,|\psi\rangle}}. \tag{1.56}$$

This can be readily generalized to density matrices where the probability of measuring outcome i is given by

$$p(i|\hat{\rho}) = \text{Tr}\,\widehat{P}_i\hat{\rho} \tag{1.57}$$

and the post-measurement state is

$$\hat{\rho}_{\text{post}} = \frac{\widehat{P}_i\hat{\rho}\widehat{P}_i}{\text{Tr}\,\widehat{P}_i\hat{\rho}} \tag{1.58}$$

When the orthogonality condition on these projection operators is relaxed, it constitutes a generalized measurement. The most general class of measurements in quantum mechanics are described in terms of positive operator-valued measures (POVMs). A POVM constitutes a set of positive semi-definite Hermitian matrices, $\{F_i\}$ which satisfy the completeness relation.

$$\sum_i \widehat{F}_i = \mathbb{I}$$

Most measurements in experiments are not perfect projective measurements. Generalized measurements help us describe such measurements mathematically. A rigorous mathematical formalism for the measurement process has been developed [198]. We shall use a particular form of generalized measurements in Chapter 3 to control the state of a particle in a harmonic trap.

1.3 Scope of the present work

The spectrum and its statistical properties have received the most attention in studies on quantum chaos (see Section 1.2.4). We pose a different question: What is the character of dynamics in such systems? Are there distinct signatures in the quantum dynamics for parameter values at which the corresponding classical system is chaotic? Are there forms of dynamics in such systems that are yet unexplored?

The interpretation of a wave function in the position basis is that the square of its absolute value is the probability density of a position measurement[199]. Since a measurement in quantum mechanics changes the state of the system, the notion of probability density is valid only in the case of an ensemble of identically prepared systems. In contrast, we ask: If the same system is repeatedly measured, what distribution would the measurement outcomes follow? In the particular case of a quantum harmonic oscillator, what form does this limiting distribution take?

Models of objective collapse (see Section 1.2.9) generally ascribe the collapse process to intrinsic stochasticity or to the presence of external fields. The Copenhagen interpretation places a nebulous dividing line between the classical and quantum realms. All collapse processes occur when the two realms talk to each other. We look into the prospects of taking this split seriously. In particular, we imagine a situation where interaction between a macroscopic and a quantum object might cause the quantum object to collapse. Without considering any particular form for this interaction, and assuming it to be local, we ask: What are the repercussions of such interaction-induced collapse processes?

1.4 Organization of the thesis

In Chapter 2 of this thesis, we delve into the realm of quantum dynamics. We choose a system: the forced impact oscillator, which is known to be classically chaotic. We investigate the dynamics of the corresponding quantum system. Unlike its classical counterpart, it is incapable of displaying chaos. Even though an isolated quantum system cannot exhibit sensitive dependence on initial condition, we show that strange nonchaotic dynamics can occur in this quantum system.

Chapter 3 deals with the statistical properties of repeated measurements on a quantum system, in particular, the quantum harmonic oscillator. The harmonic oscillator potential is chosen because of its analytical ease and importance. Through numerical experiments and analytical calculations, we show that the measurement record limits to a stable distribution. Remarkably, the limiting distribution is Gaussian, and we derive the analytical form of this limiting distribution. Furthermore, we provide analytical expressions for the mean and standard deviation of the distribution, demonstrating that periodic measurements can be used to modify and control the oscillator. Our exact results on the effects of periodic measurements of a harmonic oscillator enrich our understanding of the statistical behavior of quantum measurements in possibly the most well-studied potential in physics.

In Chapter 4 we explore the consequences of interaction-induced wave-function collapse. The Copenhagen interpretation proposed a shifty split between the macro and micro worlds. The split is unsettling as it is not guided by any physical criteria and is to be decided on a case-by-case basis at the discretion of the practicing physicist. We look into the consequences of such a split by proposing specific collapse mechanisms triggered by the interaction with macroscopic objects. Through numerical simulation, we explore the repercussions of such a hypothesis and the implications it has for the quantum world. We highlight areas where our posited model would start to deviate from quantum mechanical predictions and suggest experiments to check for the same.

We conclude in Chapter 5 and provide future directions.

This thesis weaves together four distinct research works, each offering a unique perspective on quantum dynamics, collapse mechanisms, and measurement statistics. Our findings not only advance our understanding of the quantum world but also challenge existing paradigms, providing new insights into chaos, measurement, and the fundamental laws that govern quantum systems. By delving into these interconnected topics, we contribute to the ongoing discourse surrounding the fundamental nature of quantum systems.

Chapter 2

Strange non-chaotic dynamics in a quantum system

2.1 Introduction

Bohr's correspondence principle states that quantum systems should limit to classical behavior in the appropriate macroscopic limit. Going in the reverse direction, it is reasonable to expect that classical systems with unique dynamical features could have interesting dynamical signatures in the quantum limit. Deterministic dynamical chaos is one such feature of classical systems that has been shown to have distinct features in the quantum limit. Such study has given rise to many models, distinguished among which are the 2D billiards [200–203] and δ-kicked systems [204–209]. Classical systems with a one dimensional configuration space can be chaotic, provided they are driven [210]. Although there have been some studies on quantum analogs of such classical chaotic systems [211–216], little has been explored about driven systems in piecewise smooth potentials.

Impacting systems with piecewise-smooth potentials have a unique route to chaos, marked by a sudden transition from a periodic orbit to a chaotic orbit at grazing (ie. zero velocity impacts), prompting us to ask: *what unique dynamical features do impacting classical systems exhibit in the quantum limit?* We use a simple model system to probe this question.

Simple model systems are one of the cornerstones for understanding any discipline. Paradigmatic models like the harmonic oscillator for integrable systems or the Ising model in statistical mechanics help us deepen our understanding without unnecessary complications. In a similar vein, we probe our question using a simple model system.

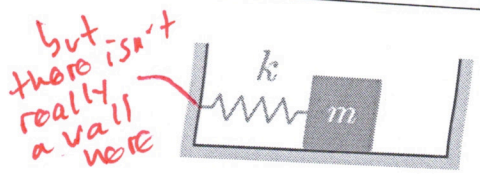

Figure 2.1: Schematic diagram of the simple impact oscillator.

2.2 The classical impact oscillator

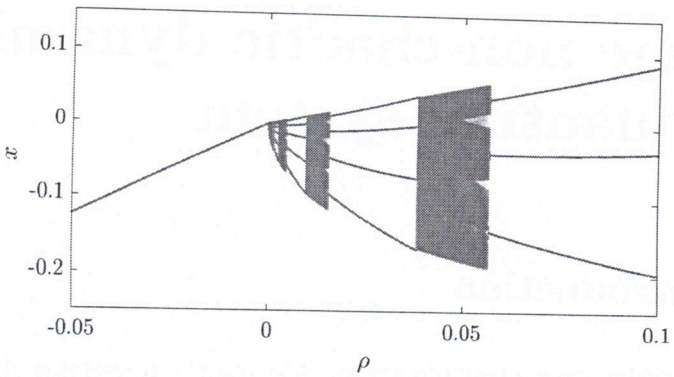

Figure 2.2: Grazing bifurcation of the Nordmark map with $\gamma = 0.05$ and $\alpha = 0.65$ [217].

The system used in this chapter is the impact oscillator comprising a mass-spring system with sinusoidal forcing (Fig. 2.1), where the mass has a possibility of impacting a wall. With dissipation, such a system exhibits a sudden onset of a large amplitude chaotic oscillation when the mass grazes the wall. This type of bifurcation, called a *grazing bifurcation* was studied by Nordmark [218] in terms of a stroboscopic map

$$\begin{cases} x_{n+1} &= \alpha x_n + y_n + \rho \\ y_{n+1} &= -\gamma x_n \end{cases} \qquad \text{for } x_n \leq 0$$

$$\begin{cases} x_{n+1} &= -\sqrt{x_n} + y_n + \rho \\ y_{n+1} &= -\gamma \tau^2 x_n \end{cases} \qquad \text{for } x_n > 0$$

where γ and α capture the characteristics of the oscillator dependent on the spring constant, the mass, and the forcing frequency. τ^2 is the coefficient of restitution of the impacts and ρ is related to the amplitude of external forcing. This simplified map captures the dynamics near the grazing condition and

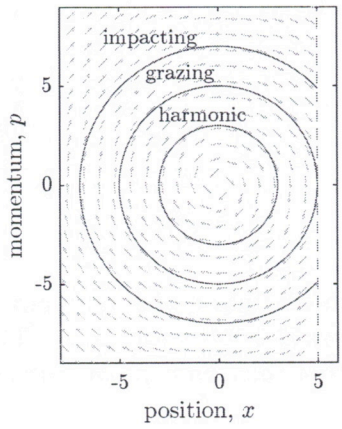

Figure 2.3: Phase space trajectories of the simple impact oscillator. The grazing trajectory divides the phase space into two dynamically distinct regions.

shows a direct transition from periodic to chaotic dynamics when the phase-space trajectory grazes the wall in the corresponding continuous-time system (see Fig. 2.2) [219, 220]. Similar phenomena are observed if the system has no damping. We explore the behavior of this system in the quantum domain.

doesn't this system have no damping?

The simple impact oscillator (without forcing and damping) is modeled as a point mass moving in the potential

$$V(x) = \begin{cases} \frac{1}{2}kx^2 & \text{if } x < x_w \\ \infty & \text{if } x \geq x_w \end{cases} \tag{2.1}$$

where x is the position of the mass ($x = 0$ corresponds to the unstretched position of the spring), and x_w is the position of the wall.

The equation of motion for the mass is given by a pair of coupled first order differential equations

$$\dot{x} = v, \qquad \dot{v} = -\frac{k}{m}x \tag{2.2}$$

Each phase space trajectory of the impact oscillator is a periodic orbit (Figure 2.3) with a unique energy. The orbit which just grazes the wall is special as it divides the phase space into two dynamically distinct regions. Orbits with energy less than the grazing orbit never touch the wall and have the same time-period as the grazing orbit, while orbits with higher energy impact the wall and have progressively shorter periods.

This classical system is decidedly not chaotic. But there is stretching in the phase space , i.e., nearby initial conditions move away from each other

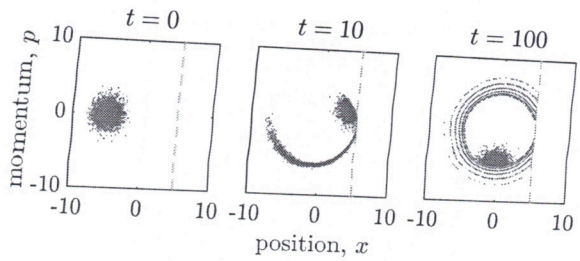

Figure 2.4: Frames from the evolution of a normally distributed ensemble of initial conditions in a classical impact oscillator. The initial conditions are taken as distributed such that the mean system satisfies the grazing condition $\langle x(0) \rangle = -x_w$.

along the trajectories. This can be appreciated from the evolution of an normally distributed ensemble of initial conditions (Fig. 2.4). Over time, continuous stretching spreads the part of the ensemble impacting the wall into an increasingly fine spiral. We shall explore the dynamics of the quantum analog of this system in the following section.

2.3 The quantum impact oscillator

We construct a quantum analog of the simple impact oscillator by using the same potential as equation (2.1) to give the Hamiltonian

$$H = -\frac{\hbar^2}{2m}\frac{\mathrm{d}^2}{\mathrm{d}x^2} + V(x) \tag{2.3}$$

with domain

$$\mathcal{D}(H) = \left\{ \begin{array}{l} \phi \mid \phi, H\phi \in \mathcal{L}^2(-\infty, x_w], \\ \phi(x_w) = \lim\limits_{x\to-\infty} \phi(x) = \lim\limits_{x\to-\infty} \phi'(x) = 0 \end{array} \right.$$

A minimum uncertainty Gaussian wavepacket serves as the initial state, with its mean at x_0 (Figure 2.5):

$$\psi(x, t=0) = \frac{1}{\sqrt[4]{2\pi}\sqrt{\sigma_0}} \exp\left\{ -\left(\frac{x - x_0}{2\sigma_0} \right)^2 \right\} \tag{2.4}$$

Closed-form solutions for the quantum impact oscillator exist only for $x_w = 0$. Hence, the time evolution was computed numerically.

The position coordinate was discretized into 10,000 steps in the range between -60 and x_w. Eigenvalues E_n and eigenvectors $|\phi_n\rangle$ of the system

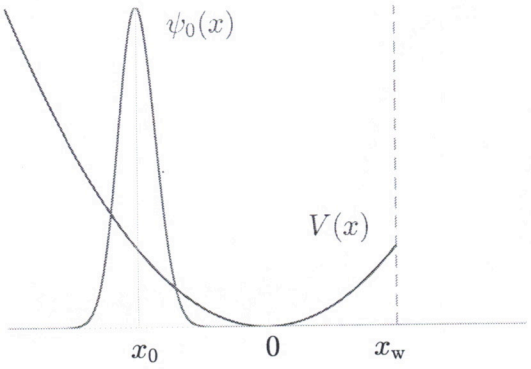

Figure 2.5: Potential function $V(x)$ and the initial wavefunction $\psi(x,0)$.

were computed by employing the Numerov-Cooley scheme [221–223]. The results were verified by directly diagonalizing the Hamiltonian matrix [223]. The initial wavefunction $\psi(x,0)$ could then be expressed in the energy basis, and its time-evolution written down as a sum of its components along the evolving energy eigenvectors.

$$\psi(x,t) = \sum_n \langle \phi_n | \psi(x,0) \rangle \; e^{-iE_n t/\hbar} \; |\phi_n\rangle$$

The above infinite series was truncated at $n = 40$ as the contribution from higher eigenvectors is well below machine precision (Fig. 2.6).

We have also calculated the evolution of the wavefunction using the time-evolution operator

$$\hat{U}(t) = \exp\left\{\frac{-i\hat{H}t}{\hbar}\right\},$$

and have checked that both the methods give the same result. The parameters were taken as $k = 1$, $m = 1$. We have used natural units with $\hbar = 1$. The initial Gaussian wavepacket has its mean at $x = -5$, hence the wall position, $x_w = 5$ corresponds to the grazing condition for the classical oscillator.

The Wigner distribution

$$W(x,p) = \frac{1}{\pi\hbar} \int_{-\infty}^{\infty} \psi^*(x+y)\, \psi(x-y)\, e^{2ipy/\hbar}\, \mathrm{d}y \tag{2.5}$$

is the quantum analog for the probability distribution over the classical phase space. Comparison of the evolution of the Wigner quasi-probability distribution for the quantum system and the evolution of a ball of initial conditions

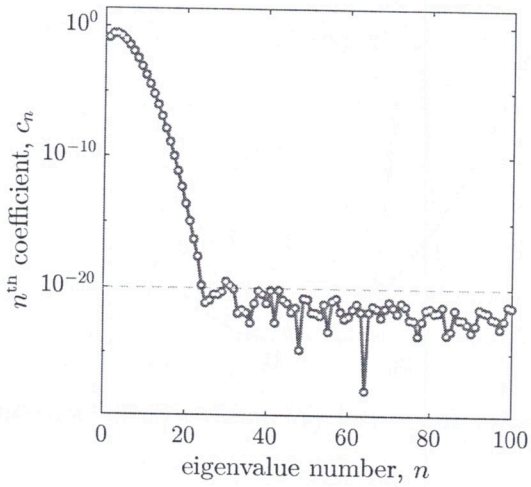

Figure 2.6: The components of the initial wavefunction (ψ_0) along the different eigenvectors (ϕ_n), given as $c_n = \langle \phi_n | \psi_0 \rangle$. It shows that components beyond $n = 40$ have negligible contribution.

in the classical system provides valuable information about the difference between the two systems. The occurrence of negative values in the quasi-probability distribution indicates a departure from classical behavior. It can be seen that definite patterns emerge in the Wigner distribution (Fig. 2.7) which evolve aperiodically. This phenomenon becomes more pronounced in the vicinity of the grazing condition.

In order to investigate the dynamical features, we need to obtain a real-valued time-series out of the complex valued wavefunction distributed in space. We employ the entropy of the probability density [224] at time t:

$$S(t) = -\int_{-\infty}^{\infty} |\psi(t,x)|^2 \log\big(|\psi(t,x)|^2\big)\, \mathrm{d}x \tag{2.6}$$

This time-series captures the nature of dynamics—it is a periodic function for a periodic evolution of the wavefunction and aperiodic otherwise. We chose entropy as the dynamical variable after trying out possible alternatives like autocorrelation, Haussdorff distance, L_n-norm for different n, and expectation values of position and momentum. Some of the measures, for instance the autocorrelation and Haussdorff distance, etc. [225] compare the wavefunction at the current instant to an earlier instant, becoming dependent on the choice of the initial wavefunction. On the other hand, the fluctuations in the expectation values of position and momentum die down to very small values as a result of the Wigner function spreading out over

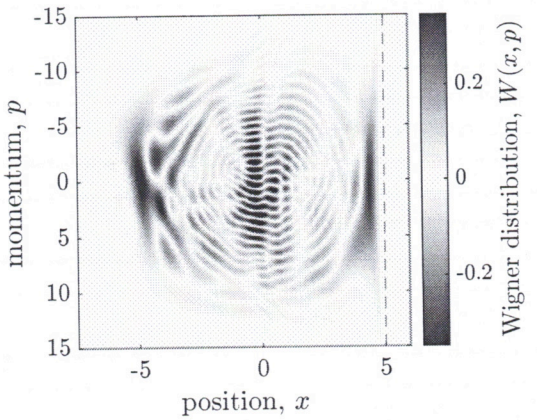

Figure 2.7: A snapshot of the evolving Wigner distribution for the grazing condition at $t = 100$.

the accessible phase space, rendering them inappropriate for characterizing the dynamics. We found that the real valued time-series of the entropy and L_1-norm capture the motion of the wavepacket indefinitely without requiring comparison with its past history.

When the wall is far away (see Fig. 2.8), we find that the entropy time-series is periodic. As the wall is moved closer, the dynamics becomes aperiodic. This is even more apparent from the frequency spectrum. It shows a collection of isolated peaks which greatly increase in number near the grazing condition. This is in stark contrast to the classical impact oscillator, which is always periodic.

We used the 0-1 test to ascertain whether the aperiodicity is due to dynamical chaos. The 0-1 test is a procedure [68] to distinguish between chaotic and non-chaotic time-series. It returns a value of 0 for periodic or quasi-periodic time-series and a value of 1 for chaotic time-series. It is known that for strange nonchaotic dynamics, the 0-1 test returns a value between zero and one [76, 77]. More details about the test are provided in Chapter 1.

We obtained values close to zero for all positions of the wall. This indicates an absence of chaos in the time-series. Sensitivity to change in initial condition is also checked by taking two close initial wavefunctions (two Gaussian functions with the same standard deviation, but slightly different means) and calculating their time-series. The trajectories do not diverge from each other. This agrees with our theoretical expectation that a closed quantum system cannot have sensitive dependence on initial conditions.

Is it then strange non-chaotic dynamics? Since the system is conservative, there cannot be any attractor. The 0-1 test was modified to robustly

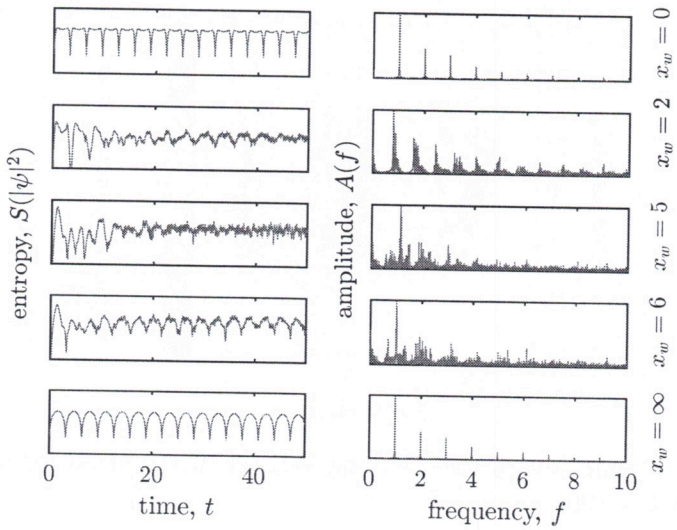

Figure 2.8: Left: entropy of the probability density $|\psi(t)|^2$ versus time for different wall positions. Right: frequency spectrum of the entropy time series.

differentiate between quasiperiodic, strange-nonchaotic and chaotic dynamics by (a) the addition of a small noise term [76], and (b) by restricting the value of c to suitable irrational numbers, particularly $c = (2\pi)^2/\omega$ where $\omega = (\sqrt{5}-1)/2$ [77]. We used the second algorithm and obtained a value close to 0. We conclude that the aperiodicity in the entropy time-series is

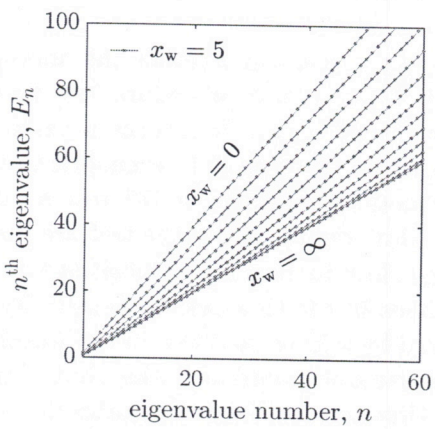

Figure 2.9: Energy spectrum for different wall positions. Except for the conditions $x_w = 0$ and $x_w = \infty$, the other energy levels grow nonlinearly with quantum number n. A typical example, $x_w = 5$, is highlighted.

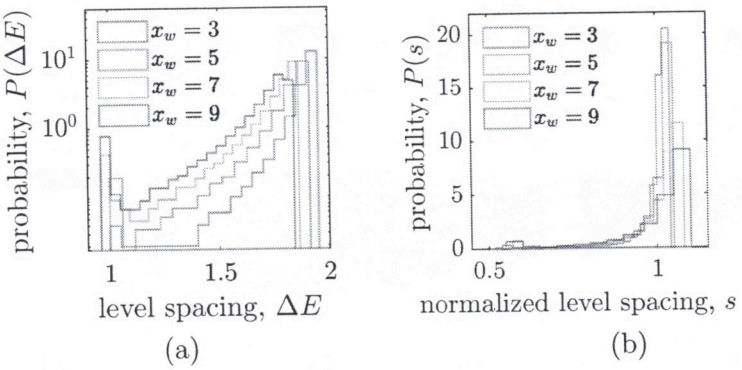

Figure 2.10: (a) Probability distribution of consecutive level spacings for different wall positions is plotted on a semi-log graph. Two prominent peaks at $\Delta E = 1$ and 2 correspond to the harmonic and half-harmonic limits. The peak at $\Delta E = 1$ decays and then grows exponentially to the peak at $\Delta E = 2$. (b) Normalized level spacing distribution for the same wall positions.

due to quasiperiodicity.

According to the Bohigas-Giannoni-Schmit conjecture [105], the statistical properties of the energy levels of a quantum system hold important information about the type of dynamics it undergoes. The energy levels of the quantum impact oscillator for different wall positions, computed using the Numerov-Cooley algorithm, is plotted in Fig. 2.9. The levels for one particular wall value ($x_w = 5$) has been highlighted to make it easy to notice its salient features. Analytical results for the cases $x_w = 0$ (half-harmonic oscillator) and $x_w = \infty$ (harmonic oscillator) are known. In the limit of large wall position, the lower energy levels approach the harmonic oscillator's energy levels $E_n = \hbar\omega\left(n + \frac{1}{2}\right)$, as their corresponding eigenfunctions are sufficiently far away from the wall to feel its presence. For large energy values, the energy levels asymptotically approach a straight line. These asymptotic limits are connected by a smooth bend. Accordingly in the level spacing distribution, we anticipate two peaks corresponding to the slope of these two asymptotic limits (see Fig. 2.10(a)).

The numerical result belies the fact that there is a maximum in the distribution at $\Delta E = 2$ for all wall positions. The numerical result shows the peaks at values less than 2 which is an artefact caused by the limitation of considering a finite number of energy levels. Dean [226] has derived a series solution for the energy levels of this system:

$$E_i(x_w) = -\frac{1}{2} + a_0(i) + a_1(i)x_w + a_2(i)x_w^2 + \cdots \tag{2.7}$$

this is the ω of the oscillator $\omega = \sqrt{\frac{k}{m}} = 1$, so it is not the same as the ω on the previous page

$E_n = \hbar\omega(n+\frac{1}{2})$ is also a straight line, so what you mean is a different straight line ~~(same with zero intercept I think)~~ with slope $2\hbar\omega$

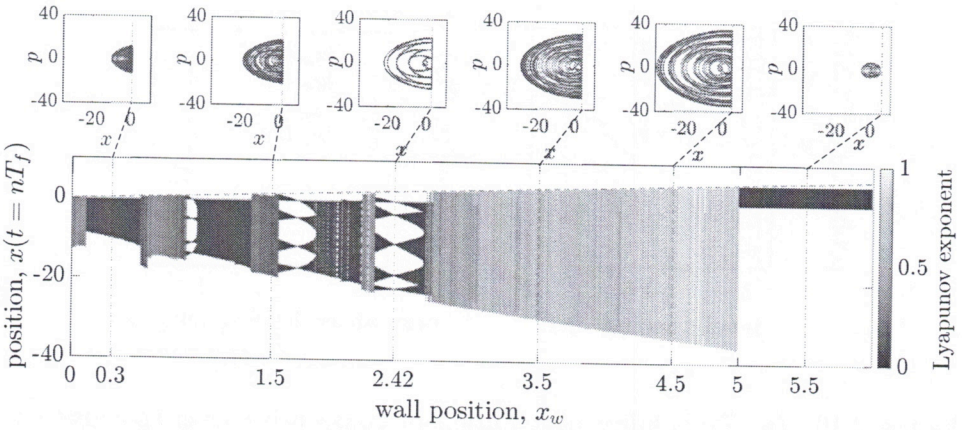

Figure 2.11: Bifurcation diagram of the classical forced impact oscillator as a function of wall position. Color indicates the Lyapunov exponent.

with

$$
\begin{aligned}
a_0(n) &= -(2n+1) \quad (n = 0, 1, 2, \cdots), \\
a_1(0) &= -\sqrt{\frac{2}{\pi}}, \\
a_1(n+1) &= \left(\frac{2n+3}{2n+2}\right) a_1(n), \\
a_2(0) &= -\frac{2}{\pi}(1 - \ln 2), \\
a_2(n+1) &= \left(\frac{2n+3}{2n+2}\right)^2 a_2(n) + \frac{(2n+3)!(2n+2)!}{16\pi[(n+1)!]^4(n+1)2^{4n}},
\end{aligned}
$$

and so on, which can be seen to limit to $\Delta E = 2$ as n approaches ∞.

It is customary to plot the distribution against the normalized level spacings, $s = \Delta E/\langle \Delta E \rangle$ (Fig. 2.10(b)). The level spacing distribution of most integrable systems is believed to be the Poisson distribution as conjectured by Berry and Tabor in [106], while classically chaotic systems are conjectured to follow Wigner-Dyson statistics. The level spacing distribution of the quantum impact oscillator is found to not satisfy this conjecture.

2.4 The Forced Impact Oscillator

The forced impact oscillator, in addition to the mass-spring-wall arrangement, has a periodic forcing acting on the mass. The classical equation of

motion for this system can be expressed as two coupled first order differential equations

$$\dot{x} = v, \qquad \dot{v} = -\frac{k}{m}x + f(t) \tag{2.8}$$

In this work we confine ourselves to the case of sinusoidal forcing of the form:

$$f(t) = A_f \sin \omega_f t$$

The bifurcation diagram (Fig. 2.11) for the system shows that the addition of forcing makes the system chaotic in certain ranges of the wall position. It also shows the sudden appearance of a large amplitude orbit at the grazing condition ($x_w = 5$). There are windows of chaos, quasiperiodicity and periodicity for different wall positions. The Poincaré section (Fig. 2.12) obtained for wall position $x_w = 3$ shows a mixed phase space with chaotic and regular regions entangled in a complicated manner.

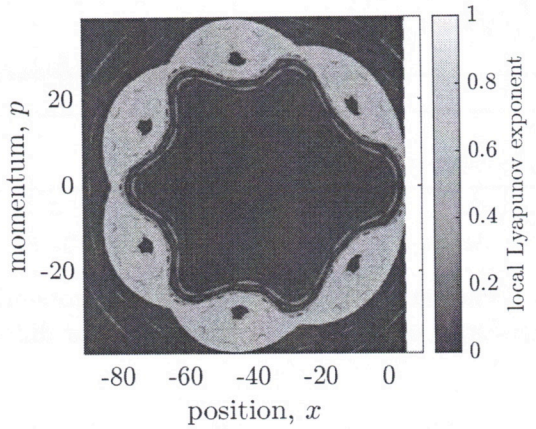

Figure 2.12: Poincaré section of the classical forced impact oscillator for $A_f = 20$, $\omega_f = \frac{\sqrt{5}+1}{2}$, $k = 1$, $m = 1$ and the wall position is 5. The colors indicate the finite-time Lyapunov exponent of the trajectory near the corresponding point.

2.5 Quantum Forced Impact Oscillator

The quantum forced impact oscillator is constructed by adding a forcing term to the potential

$$V(x,t) = V_0 + xA_f \sin(\omega_f t),$$

where V_0 is the static potential of the impact oscillator, given by (2.1). The initial state is taken to be a coherent-width Gaussian wavepacket with mean at $x = 0$ and variance $\frac{\hbar}{2\sqrt{km}}$. The natural frequency of the harmonic oscillator without the wall is 1, and the forcing frequency is taken as an irrational number, the golden ratio $\frac{\sqrt{5}+1}{2}$. The system is numerically simulated by first representing the initial wavefunction in the energy basis of the static Hamiltonian, and then evolving it using adaptive timestep 4th order Runge-Kutta method [227]. The entropy time-series is used as a probe for the nature of dynamics.

what value for A_f?

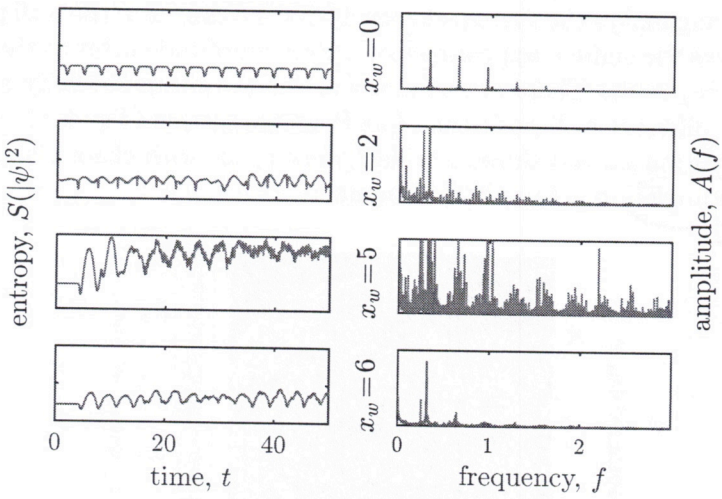

Figure 2.13: Left: Time-series of the entropy of the probability distribution. Right: Fourier transforms of the entropy time-series for different positions of the wall.

The entropy plots of the system for different wall positions are shown in the left side of Fig. 2.13. The frequency spectra are plotted to the right. For wall position $x = 0$, the entropy plot is periodic and its Fourier transform shows the forcing frequency and its harmonics.

For wall positions where the wavefunction interacts with the wall, we see aperiodic dynamics. The Fourier transform plots show a large number of peaks. As the wavefunction is an extended entity in space, the grazing condition cannot be defined as in the classical case. To find the grazing condition, we remove the wall and observe the dynamics of the coherent state in the (now) harmonic potential subjected to the same sinusoidal driving. We allow the time evolution to reach a steady state of oscillation. The conditions for which the peak of the coherent state just reaches the position where the wall used to be, is taken to be the grazing condition for the quantum impact

oscillator. For $x_w = 5$ and $\omega_f = \frac{1+\sqrt{5}}{2}$ we find the condition for grazing is $A_f = 0.015$. Remarkably, we see a very large number of discrete frequency components at the grazing condition. In all cases, we see the presence of two peaks at the natural and forcing frequencies. The situation with the wall moved to infinity is not presented in the figure as the entropy remains constant.

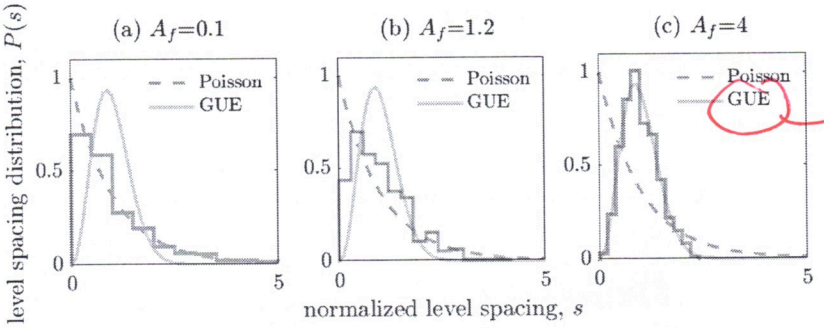

not GOE, comment on lack of time-reversal symmetry ($t \to -t$ reverses $\sin(\omega t)$)

Figure 2.14: Level spacing distribution of the Floquet quasi-energy spectrum for the forced impact oscillator with wall position $x_w = 5$, forcing frequency $\omega_f = 1 + \frac{\sqrt{5}}{2}$, with forcing amplitudes (a) $A_f = 0.1$, (b) $A_f = 1.2$, and (c) $A_f = 4$. The distribution transitions from Poission to GUE as the forcing amplitude is increased.

The normalized level spacing distribution of the Floquet quasi-energy spectrum for the forced impact oscillator is shown in Fig. 2.14. The distribution can be seen to follow the Poisson distribution when the amplitude of forcing is small ($A_f = 0.1$) as is predicted by the conjecture of Berry and Tabor in [106]. With increase in the forcing amplitude, the distribution transitions smoothly into a Gaussian Unitary Ensemble (GUE) in accordance to the BGS conjecture [105] regarding the level-spacing distributions of integrable and chaotic systems respectively.

how many states? what range of energies? surprising that it matches GUE for $A_f = 4$ when $A_f = 20$ shows a mixed classical phase space (Fig 2.17)

A bifurcation diagram for the average quantum probability density at different wall positions is plotted in Fig. 2.15. When the wall is far away, the wavefunction cannot interact with the wall and undergoes periodic motion in the harmonic well at the forcing frequency. As the wall is moved closer, the wavefunction gets partially reflected at the wall and interferes with itself resulting in large amplitude banded patterns. This pattern occurs over a range around the point of grazing ($x_w = 5$). This is reminiscent of the large amplitude chaotic orbit appearing at the grazing condition for the classical system (Fig. 2.11).

averaged over one driving cycle?

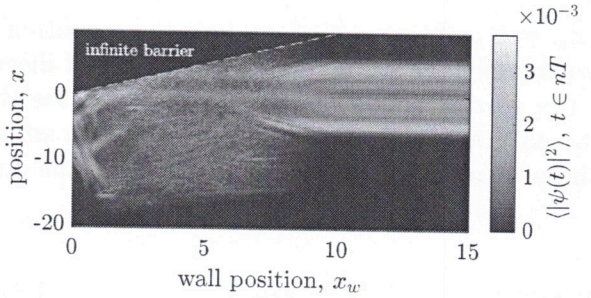

Figure 2.15: The quantum bifurcation diagram for the forced impacting system.

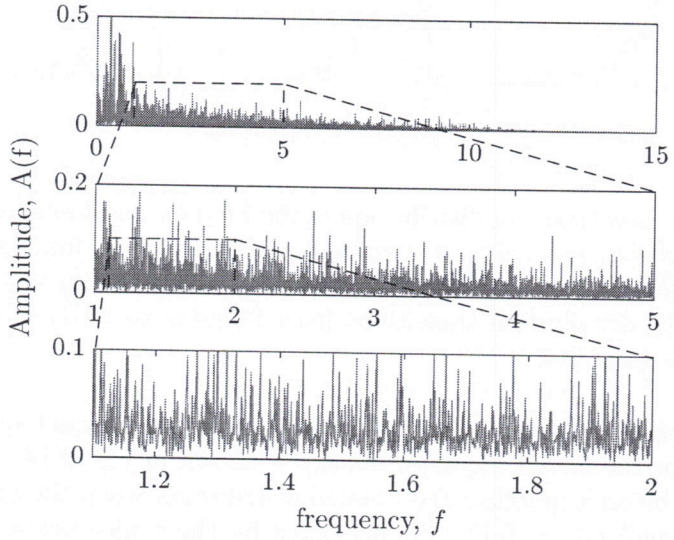

Figure 2.16: Two consecutive zooms of the frequency plot corresponding to Fig. 2.13, the case of $x_w = 5$.

Signatures of strange non-chaotic behavior

The increase in the number of frequency components for a range of parameter values (Fig. 2.13) alerted us of the possibility of strange non-chaotic behavior. We use three diagnostic tests to check the character of the time-series that we obtained for the grazing condition.

Bezhaeva and Oseledets [228] showed that a dense set of discrete peaks occurs in the Fourier spectrum of the time-series obtained from a strange orbit. Two consecutive zooms of the frequency plot of the quantum impact

oscillator for the grazing condition is shown in Fig. 2.16. It indicates a dense set of frequency peaks with a fractal character. Such fractal quasienergy spectrum have been observed in previous studies in quantum chaos [206, 229–231].

It is also known that the Fourier spectrum of the time-series of a strange orbit has a certain characteristic scaling behavior [63, 79]. The spectral distribution function, i.e., the number of peaks with amplitude larger than a threshold plotted against the threshold (see Fig. 2.17), has a power-law relationship in the case of strange attractors.

The spectral distribution function for the entropy time-series of the classical impact oscillator is plotted in a log-log scale in Fig. 2.18(a). It shows power law characteristics ($N(\sigma) = 51520\,\sigma^{-0.67}$), indicating the strange character of underlying the phase space flow. The spectral distribution function of the quantum system plotted in a log-log scale (Fig. 2.18(b)) exhibits power-law character with two characteristic scaling exponents

$$\begin{aligned} N(\sigma) &= 9.593\,\sigma^{-4.293} \quad \text{for } \sigma \in [2, 3.67] \\ N(\sigma) &= 3422.1\,\sigma^{-8.658} \quad \text{for } \sigma \in (3.67, 7.7], \end{aligned}$$

implying a strange character of the dynamics.

It is known that, even though the largest Lyapunov exponent for a strange nonchaotic orbit is negative, the dynamics can be locally unstable [79]. This is captured by the stationary density of finite-time Lyapunov exponents [232, 233]. The presence of positive values in this distribution indicates that the dynamics is locally unstable [62, 63].

The stationary density of finite-time Lyapunov exponents for the quantum impact oscillator at the grazing condition is shown in Fig. 2.19. The

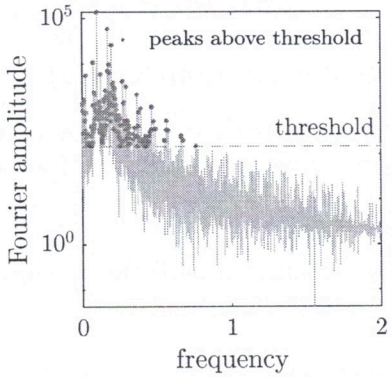

Figure 2.17: An illustration of the spectral distribution function. It counts the number of frequency components greater than a threshold.

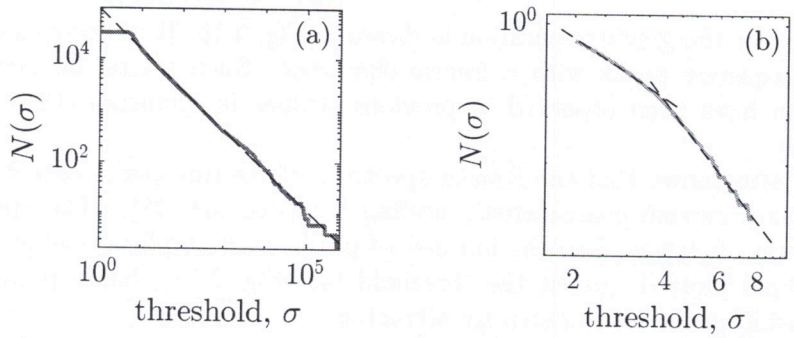

Figure 2.18: Spectral distribution function, i.e., the number of peaks above threshold σ versus the threshold (a) for the classical system at the grazing condition, plotted in log-log scale, (b) for the forced quantum impact oscillator entropy time-series in log-log scale.

presence of positive values in this distribution indicates the occurrence of strange nonchaotic dynamics.

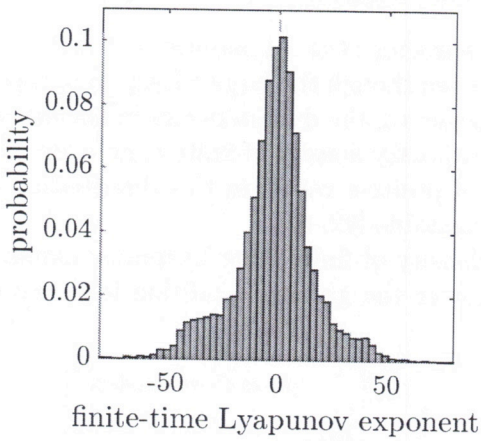

Figure 2.19: Distribution of finite-time Lyapunov exponents of the entropy time-series. Presence of positive parts indicates fractal structure of the underlying dynamics.

In order to be doubly certain, we used the L_1-norm of the wavefunction as another dynamical variable

$$||\psi(t,x)||_1 = \int_{-\infty}^{\infty} |\psi(t,x)|\,\mathrm{d}x \tag{2.9}$$

which also yields a positive real number. The findings from the L_1-norm

time-series are similar to those from the entropy time-series

Measure	0-1 test(K)	Modified 0-1 test (K)
Entropy	0.86	0.45
L_1-norm	0.69	0.69

Table 2.1: Results of 0-1 test and modified 0-1 test for the entropy and L_1-norm time-series at the grazing condition.

Table 2.1 shows the results of the 0-1 test for chaos and modified 0-1 test (as described in [77]) when applied to the entropy and L_1-norm times series. It has been reported in [77, 234] that intermediate values between 0 and 1 indicate the presence of strange nonchaotic dynamics.

2.6 Conclusions

In this chapter we have explored the quantum dynamics of a classically chaotic system, the impact oscillator. The classical system transitions into a chaotic behavior when the mass just grazes the wall. In the quantum analog, the wavefunction interacts with the wall even before the classical grazing condition and the wavefunction is found to evolve aperiodically over a range of the position of the wall.

The diagnostic tests performed on the entropy time-series extracted from the evolution of the wavefunction show that for the unforced quantum impact oscillator the dynamics is quasiperiodic, while that of the classical system is periodic. The level spacing distribution follows neither Poisson nor the Wigner-Dyson distribution.

For the forced quantum impact oscillator, the dynamics has all the characteristic features of a strange nonchaotic orbit. The frequency spectrum is discrete but dense. The distribution of finite-time Lyapunov exponents has positive components while the long-term Lyapunov exponent is negative. Two forms of the 0–1 test yield values between 0 and 1. The spectral distribution function has a power-law character with two different exponents for different ranges of threshold. This establishes that the behavior is strange but not chaotic.

The quasi-energy level spacings are found to transition from Poisson distribution to GUE, as the fraction of the classical phase space populated by chaotic orbits increases. This is in accordance to the conjectures of Berry-Tabor and Bohigas-Giannoni-Schmit.

We have repeated our analysis on quantum analogs of different forced oscillators: the forced pendulum, undamped Duffing oscillator and the Kapitza

the impact oscillator is not chaotic (did you mean the forced impact oscillator?)

pendulum. We report that none of these systems show signs of strange nonchaotic dynamics. In that sense our observations in the forced impact oscillator are atypical.

To our knowledge this work provides the first numerical evidence for strange nonchaotic dynamics in a quantum system. The existence of this novel dynamics could have important applications in quantum information and related technologies. Rigorous justification for the existence of this form of dynamics in quantum systems is still an open problem.

Chapter 3

Limiting distribution of periodic position measurements of a quantum harmonic oscillator

3.1 Introduction

Quantum theory is perfectly deterministic except when a measurement is made. The outcomes of measurements in quantum mechanics are probabilistic. The probabilities are given by Born's rule, which states that the square of the modulus of the wavefunction is the probability density of the measurement outcome. If we take an ensemble of identically prepared quantum systems, the distribution of measurement outcomes would follow Born's rule. We ask a different question: What is the distribution of measurement outcomes when the *same* quantum system is periodically measured?

Our aim in this chapter is to characterize the statistical distribution of a sequence of position measurements of a quantum system. We consider a particle in a harmonic oscillator potential, whose position is periodically measured with an instrument of finite precision. We choose the quantum harmonic oscillator because it approximates the neighbourhood of the minima of any smooth potential well.

We show that the distribution of the measured positions tends to a limiting distribution when the number of measurements tends to infinity. We derive the expression for the limiting position distribution and validate it with numerical simulation.

should appear on or after page where first referenced

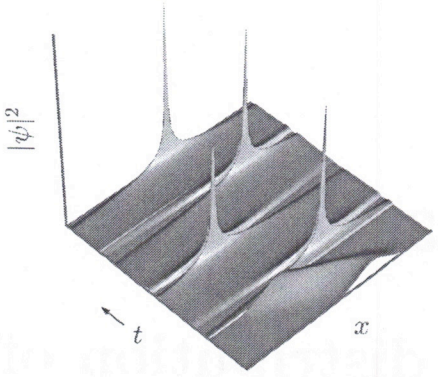

Figure 3.1: Evolution of the probability density function with periodic measurement

3.2 Problem Statement

A particle is placed in a harmonic oscillator potential

$$V = \frac{1}{2}m\omega^2 x^2. \tag{3.1}$$

The particle is initially in a state $\Psi(x, 0)$ and we subject it to periodic measurements at intervals of time t_M. When a position measurement is made, the wavefunction is supposed to collapse to a delta function, whose position would be a random number following the probability distribution given by the wavefunction just before the collapse. Subsequently, the wavefunction would evolve following the Schrödinger equation until the next observation.

only if the measurement has infinite precision

In order for the above scheme to work in numerical simulation, we need the wavefunction to be smooth. So we consider the state immediately after a collapse to be a narrow Gaussian function centered at x_M with standard deviation σ_M,

better justification is that all measurements have finite precision

$$\Psi(x, t_M) \xrightarrow{\text{measurement}} \mathcal{G}(x - x_M, \sigma_M). \tag{3.2}$$

In fact, it is supposed to collapse to a wavefunction which is a product of the wavefunction before measurement and the Gaussian function representing the measurement process. However, if the measurement process is represented by a Gaussian function that is narrow enough compared to the spread of the particle wavefunction, the post-collapse wavefunction can be aptly represented by the narrow Gaussian alone.

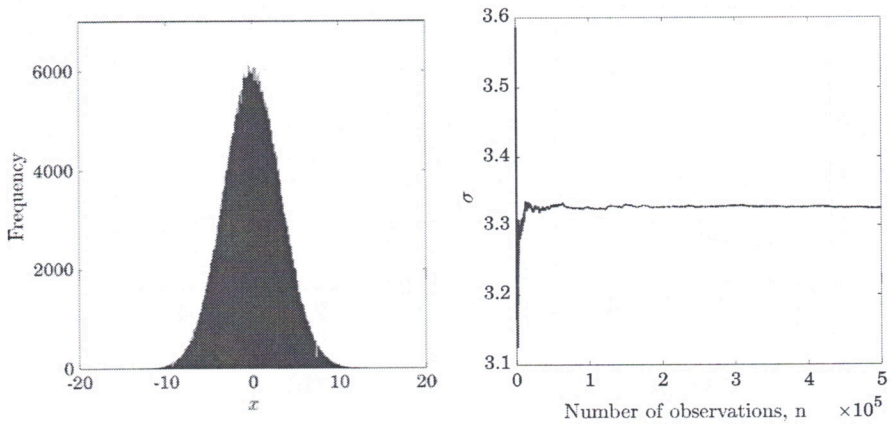

(a) (b)

Figure 3.2: (a) Histogram of 5×10^5 measurements for $m = 1$, $\omega = 0.707$, $\sigma_{_M} = 0.5$, $t_{_M} = \frac{T}{5} = \frac{2\pi}{5\omega}$, (b) Convergence of the standard deviation, which tends to σ_∞

3.3 Numerical Simulation

The system was simulated by evolving the wavefunction for $t_{_M}$ seconds and drawing a random sample $x_{_M}$ every $t_{_M}$ seconds from the probability density $|\Psi(x)|^2$ just before measurement. Just after the measurement it was replaced by a narrow Gaussian of standard deviation $\sigma_{_M}$ and centered at $x_{_M}$. The state was then allowed to evolve until the next measurement following the Schrödinger equation (Fig. 3.1). The process was repeated to obtain the limiting distribution of samples, which we plot in Fig. 3.2(a). Numerical simulations for various values of $t_{_M}$ and $\sigma_{_M}$ revealed that the limiting distribution is always Gaussian. The standard deviation of the samples was found to rapidly converge to a constant value as the number of samples was increased (Fig. 3.2(b)). This observation of convergence to a Gaussian distribution motivated our analytical approach, which is presented in section 3.5.

In order to check the dependence of the limiting standard deviation (σ_∞) on the accuracy of the measuring device, we obtained the results for different values of $\sigma_{_M}$. The results are presented in Fig. 3.3(a). Similarly, we explore the dependence of the limiting standard deviation on the natural frequency of the harmonic oscillator, which we plot in Fig. 3.3(b). We also found that the limit distribution is independent of the initial wavefunction.

The assumption of perfectly periodic measurements cannot be realized in practice. Hence, we numerically investigated the effect of a Gaussian noise

comment on results. 3.3(b) is unsurprising since the potential well gets narrower/steeper as ω increases, but 3.3(a) is unexpected (by me, at least)

not surprising since it only affects the first value of x_M

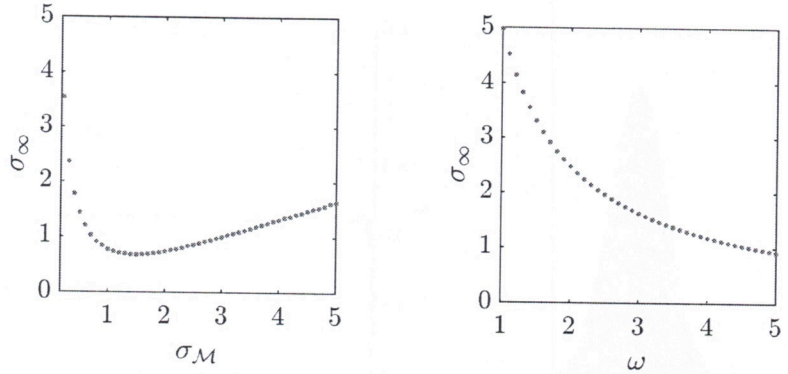

Figure 3.3: Limiting standard deviation versus (a) the standard deviation of collapsed wavefunction, and (b) the natural frequency of the harmonic oscillator.

added to the time period of measurement. We found that the additional noise has a negligible effect on the limiting standard deviation. This implies that the analytical results presented below, which are derived based on the assumption of periodic measurements, also hold for approximately periodic measurements.

Note that our measurement scheme can be described in the language of positive operator-valued measures (POVMs), which is shown in the following section. Hence, the scheme is, in principle, realizable.

3.4 A POVM reformulation of our measurement scheme

We shall demonstrate that our scheme can be realized as a generalized measurement (POVM). In particular, we show that our scheme can be reformulated as a weak position measurement, which is a subclass of generalized measurements [235].

The measurement scheme used in this chapter (3.2) is

$$\Psi(x, t_\mathcal{M}) \xrightarrow{\text{measurement}} \mathcal{G}(x - x_\mathcal{M}, \sigma_\mathcal{M}),$$

which, we shall show, is a special case of the weak measurement protocol used in [193, 196]

$$\Psi(x) \xrightarrow{\text{measurement}} \frac{1}{\mathcal{N}} \exp\left\{\frac{-(x - x_w)^2}{2\sigma_w^2}\right\} \Psi(x),$$

where σ_w is a measure of the imprecision of the instrument and x_w denotes the position registered by the instrument. $\mathcal{N}$ ensures normalization of the post-measurement state.

Equating the post-measurement states of both these schemes,

$$\mathcal{G}(x - x_M, \sigma_M) = \frac{1}{\mathcal{N}} \exp\left\{\frac{-(x - x_w)^2}{2\sigma_w^2}\right\} \Psi(x) .$$

Since the states used in this chapter are Gaussian wave packets, $\Psi(x)$ can be written as $\mathcal{G}(x - \mu_\psi, \sigma_\psi)$, which gives

$$\mathcal{G}(x - x_M, \sigma_M) = \frac{1}{\mathcal{N}} \mathcal{G}(x - x_w, \sigma_w)\, \mathcal{G}(x - \mu_\psi, \sigma_\psi) .$$

Using results about the product of two Gaussians [236], we write

$$\sigma_M^2 = \frac{\sigma_w^2 \sigma_\psi^2}{\sigma_w^2 + \sigma_\psi^2} , \qquad x_M = \frac{x_w \sigma_\psi^2 + \mu_\psi \sigma_w^2}{\sigma_w^2 + \sigma_\psi^2} .$$

Rearranging terms,

$$\sigma_w^2 = \frac{\sigma_M^2 \sigma_\psi^2}{\sigma_\psi^2 - \sigma_M^2} , \qquad x_w = \frac{x_M \sigma_\psi^2 - \mu_\psi \sigma_w^2}{\sigma_\psi^2 - \sigma_M^2} .$$

Hence, our measurement scheme is equivalent to a weak measurement with the above parameters.

3.5 Derivation of Limit Distribution

We now obtain the expression for the limiting distribution and its dependence on various parameters.

The evolution of a Gaussian wave packet in a harmonic potential is a well known result [237–239]. Let the initial wave packet be

$$\Psi(x, 0) = \frac{1}{\sqrt[4]{2\pi}\sqrt{\sigma_{x0}}} \exp\left\{\left\{-\frac{(x - x_0)^2}{4\sigma_{x0}^2}\right\}\right\}, \tag{3.3}$$

where x_0 is the initial center of the Gaussian wave packet, σ_{x0} is the initial width of wave packet. Then the probability density at time t is given by

$$|\Psi(x, t)|^2 = \frac{1}{\sqrt{2\pi}\sigma(t)} \exp\left\{\left\{-\frac{(x - x_0 \cos\omega t)^2}{2\sigma^2(t)}\right\}\right\}, \tag{3.4}$$

where

$$\sigma(t) = \frac{\sigma_{gs}^2}{2\sqrt{2}\,\sigma_{x0}} \sqrt{4\left(\frac{\sigma_{x0}}{\sigma_{gs}}\right)^4 + 1 + \left(4\left(\frac{\sigma_{x0}}{\sigma_{gs}}\right)^4 - 1\right)\cos 2\omega t} \tag{3.5}$$

and $\sigma_{gs} = \sqrt{\hbar/m\omega}$ is the width of the ground-state eigenfunction.

For the sake of succinctness, we shall refer to a Gaussian in x centered at μ with standard deviation σ as $\mathcal{G}(x-\mu, \sigma)$, whereby the time evolution of a Gaussian wavepacket can be expressed as

$$\mathcal{G}(x - x_0, \sigma_{x0}) \xrightarrow{t} \mathcal{G}(x - x_0\cos\omega t, \sigma(t)) \tag{3.6}$$

At $t = 0$ we start with a Gaussian wavepacket (3.3) centered at $x = 0$, and width σ_{x0}. We repeatedly measure the position of the particle after fixed time intervals of $t_{\mathcal{M}}$. At each measurement a random value of the position is chosen following the distribution of $|\Psi|^2$ at that time instant.

A measurement collapses the wavefunction. The imprecise instrument is assumed to collapse the wavefunction into a narrow Gaussian wavepacket

$$\Psi_i(x, 0) = \frac{1}{\sqrt[4]{2\pi}\sqrt{\sigma_{\mathcal{M}}}} \exp\left\{-\frac{(x - x_{\mathcal{M}i})^2}{4\sigma_{\mathcal{M}}^2}\right\},$$

where $x_{\mathcal{M}i}$ is the outcome of the i^{th} measurement. The next measurement happens after a time $t_{\mathcal{M}}$. The probability density for the wavefunction just before the next measurement can be calculated using equation (3.4):

$$\begin{aligned} |\Psi_i(x, t_{\mathcal{M}})|^2 &= \frac{1}{\sqrt{2\pi}\sigma(t_{\mathcal{M}})} \exp\left\{-\frac{(x - x_{\mathcal{M}i}\cos\omega t_{\mathcal{M}})^2}{2\sigma^2(t_{\mathcal{M}})}\right\} \\ &= \mathcal{G}(x - x_{\mathcal{M}i}\cos\omega t_{\mathcal{M}}, \sigma(t_{\mathcal{M}})). \end{aligned}$$

For the first measurement the distribution is

$$\begin{aligned} \mathcal{D}_1(x) &= |\Psi(x, t_{\mathcal{M}})|^2 \\ &= \frac{1}{\sqrt{2\pi}\sigma_0(t_{\mathcal{M}})} \exp\left\{-\frac{x^2}{2\sigma_0^2(t_{\mathcal{M}})}\right\} \\ &= \mathcal{G}(x, \sigma_0(t_{\mathcal{M}})) \end{aligned}$$

We denote the standard deviation of this distribution as $\sigma_0(t_{\mathcal{M}})$ to distinguish it from all subsequent standard deviations. The densities before all subsequent measurements have the same width as they all start from a collapsed state whose standard deviation is identical in all cases. The expected distribution for the second measurement is

$$
\begin{aligned}
\mathcal{D}_2(x) &= \int_{-\infty}^{\infty} \mathcal{D}_1(x_{M1})\ |\Psi_1(x, t_M)|^2\, \mathrm{d}x_{M1} \\
&= \int_{-\infty}^{\infty} \mathcal{G}\left(x_{M1}, \sigma_0(t_M)\right)\ \mathcal{G}\left(x - x_{M1}\cos\omega t_M, \sigma(t_M)\right) \mathrm{d}x_{M1} \\
&= \int_{-\infty}^{\infty} \frac{1}{\sqrt{2\pi}\sigma_0(t_M)} \exp\left\{\left\{ - \frac{(x_{M1})^2}{2\sigma_0(t_M)^2}\right\}\right\} \\
&\quad \frac{1}{\sqrt{2\pi}\sigma(t_M)} \exp\left\{\left\{ - \frac{(x - x_{M1}\cos\omega t_M)^2}{2\sigma(t_M)^2}\right\}\right\} \mathrm{d}x_{M1} \\
&= \int_{-\infty}^{\infty} \frac{1}{\sqrt{2\pi}\sigma_0(t_M)} \exp\left\{\left\{ - \frac{(x_{M1})^2}{2\sigma_0(t_M)^2}\right\}\right\} \sec\omega t_M \\
&\quad \frac{1}{\sqrt{2\pi}(\sigma(t_M)\sec\omega t_M)} \exp\left\{\left\{ - \frac{(x_{M1} - x\sec\omega t_M)^2}{2(\sigma(t_M)\sec\omega t_M)^2}\right\}\right\} \mathrm{d}x_{M1} \\
&= \int_{-\infty}^{\infty} \sec\omega t_M \mathcal{G}\left(x_{M1}, \sigma_0(t_M)\right)\ \mathcal{G}\left(x_{M1} - x\sec\omega t_M, \sigma(t_M)\sec\omega t_M\right) \mathrm{d}x_{M1}
\end{aligned}
$$

unnecessary ( ) and { }

#

σ_0, not 1

Using the following result about the integral of the product of two Gaussians

$$
\int_{-\infty}^{\infty} \mathcal{G}\left(x - \mu_1, \sigma_1\right)\ \mathcal{G}\left(x - \mu_2, \sigma_2\right) \mathrm{d}x = \quad \mathcal{G}\left(\mu_1 - \mu_2, \sqrt{\sigma_1^2 + \sigma_2^2}\right),
$$

#

we have

$$
\begin{aligned}
\mathcal{D}_2(x) &= \sec\omega t_M \mathcal{G}\left(x\sec\omega t_M, \sqrt{\sigma_0(t_M)^2 + \sigma(t_M)^2\sec^2\omega t_M}\right) \\
&= \frac{\sec\omega t_M \exp\left\{\left\{ - \frac{x^2\sec^2\omega t_M}{2\{\sigma(t_M)^2\sec^2\omega t_M + \sigma_0(t_M)\}^2}\right\}\right\}}{\sqrt{2\pi}\sqrt{\sigma(t_M)^2\sec^2\omega t_M + \sigma_0(t_M)^2}} \\
&= \frac{\exp\left\{\left\{ - \frac{x^2}{2\{\sigma(t_M)^2 + \sigma_0(t_M)\cos^2\omega t_M\}^2}\right\}\right\}}{\sqrt{2\pi}\sqrt{\sigma(t_M)^2 + \sigma_0(t_M)^2\cos^2\omega t_M}} \\
&= \mathcal{G}\left(x, \sigma(t_M)\sqrt{1 + \left(\frac{\sigma_0(t_M)}{\sigma(t_M)}\right)^2\cos^2\omega t_M}\right).
\end{aligned}
$$

#

$$\frac{\sigma^2(t_M)\left(1 + \left(\frac{\sigma_0(t_M)}{\sigma(t_M)}\right)^2\cos^4\omega t_M\right)}{\sigma(t_M)^2}$$

Similarly, for the third measurement, the density is

$$\sigma(t_M)\sqrt{1 + \left(\frac{\sigma(t_M)\sqrt{1 + \left(\frac{\sigma_0(t_M)}{\sigma(t_M)}\right)^2\cos^2\omega t_M}}{\sigma(t_M)}\right)^2\cos^2\omega t_M}$$

$$\to \sigma(t_M)\sqrt{1 + \cos^2\omega t_M + \left(\frac{\sigma_0(t_M)}{\sigma(t_M)}\right)^2\cos^4\omega t_M}$$

$$\begin{aligned}\mathcal{D}_3(x) &= \int_{-\infty}^{\infty} \mathcal{D}_2(x_{M2})\, |\Psi_2(x, t_M)|^2 \, \mathrm{d}x_{M2} \\ &= \mathcal{G}\left(x, \sigma(t_M)\sqrt{1 + \cos^2 \omega t_M + \left(\frac{\sigma_0(t_M)}{\sigma(t_M)}\right)^2 \cos^4 \omega t_M}\right).\end{aligned}$$

And for the n^{th} measurement the density is

$$\mathcal{D}_n(x) = \mathcal{G}\left(x, \sigma(t_M)\sqrt{1 + cos^2\omega t_M + \cdots + \left(\frac{\sigma_0(t_M)}{\sigma(t_M)}\right)^2 \cos^{2(n-1)} \omega t_M}\right).$$

The geometric series converges if $\cos^2 \omega t_M < 1$,

$$\begin{aligned}\mathcal{D}_\infty(x) &= \mathcal{G}\left(x, \sigma(t_M)\sqrt{1 + cos^2\omega t_M + \ldots}\right) \\ &= \mathcal{G}\left(x, \sigma(t_M)\sqrt{\frac{1}{1 - cos^2\omega t_M}}\right) \\ &= \mathcal{G}\left(x, \frac{\sigma(t_M)}{|\sin \omega t_M|}\right) \qquad (3.7)\end{aligned}$$

or,

$$\sigma_\infty = \left|\frac{\sigma(t_M)}{\sin \omega t_M}\right|. \qquad (3.8)$$

The distribution of position measurements is then the distribution of samples, one taken from each $\mathcal{D}_i$. This is the mean of the densities $\mathcal{D}_i$. So we have

$$\sigma_i^2 = \sigma(t_M)^2 + \sigma(t_M)^2 cos^2\omega t_M + \cdots + \sigma_0(t_M)^2 \cos^{2(i-1)} \omega t_M \qquad (3.9)$$

The mean of all these densities is again a Gaussian with mean at zero and variance s_∞^2 given by the mean of the individual variances given by equation (3.9).

$$
\begin{aligned}
s_\infty^2 &= \lim_{n\to\infty} \frac{1}{n} \sum_{i=1}^{\infty} \sigma_i^2 \\
&= \lim_{n\to\infty} \Big[\frac{1}{n} \sigma_0(t_M)^2 \\
&\quad + \frac{1}{n} \left\{ \sigma(t_M)^2 + \sigma_0(t_M)^2 cos^2 \omega t_M \right\} \\
&\quad \vdots \\
&\quad + \frac{1}{n} \left\{ \sigma(t_M)^2 + cos^2 \omega t_M + \cdots + \sigma_0(t_M)^2 \cos^{2(i-1)} \omega t_M \right\} \Big] \\
&= \lim_{n\to\infty} \Bigg[\frac{\sigma_0(t_M)^2}{n} \left\{ 1 + \cos^2 \omega t_M + \cos^4 \omega t_M + \dots \right\} \\
&\quad + \frac{\sigma(t_M)^2}{n} [n + (n-1)\cos^2 \omega t_M + \dots \\
&\quad + (n - (i-1)) \cos^{2(i-1)} \omega t_M + \dots \Bigg] \\
&= \lim_{n\to\infty} \frac{\sigma_0(t_M)^2 \mathrm{cosec}^2 \omega t_M}{n} + \frac{\sigma(t_M)^2}{n} \sum_{k=1}^{\infty} [n - (k-1)] (\cos^2 \omega t_M)^{(k-1)}
\end{aligned}
$$

If $\cos^2 \omega t_M < 1$ the second term is a convergent arithmetico-geometric series and we have

$$
\begin{aligned}
s_\infty^2 &= \lim_{n\to\infty} \left[\frac{\sigma_0(t_M)^2 \mathrm{cosec}^2 \omega t_M}{n} + \frac{\sigma(t_M)^2}{n} \left\{ \frac{n}{1 - \cos^2 \omega t_M} - \frac{\cos^2 \omega t_M}{(1 - \cos^2 \omega t_M)^2} \right\} \right] \\
\therefore\ s_\infty^2 &= \left\{ \frac{\sigma(t_M)}{\sin \omega t_M} \right\}^2
\end{aligned}
$$

$$
\therefore\ s_\infty = \left| \frac{\sigma(t_M)}{\sin \omega t_M} \right| = \sigma_\infty \tag{3.10}
$$

We find that s_∞ is the same as σ_∞. This means that the distribution of measurement outcomes $x_{M1}, x_{M2}, \dots, x_{Mn}$ itself converges to $\mathcal{D}_\infty$ as $n \to \infty$.

Substituting equation (3.5) in equation (3.10) we get

$$
\sigma_\infty = \left| \frac{\sigma_0^2 \sqrt{4\left(\frac{\sigma_{x0}}{\sigma_0}\right)^4 + 1 + \left(4\left(\frac{\sigma_M}{\sigma_0}\right)^4 - 1\right) \cos 2\omega t_M}}{2\sqrt{2}\, \sigma_M \sin \omega t_M} \right|
$$

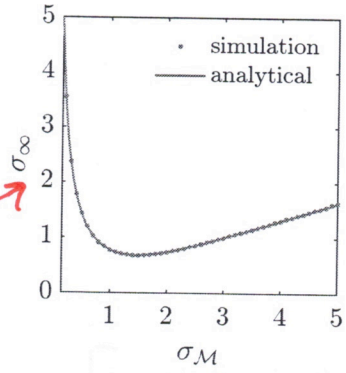

(a)

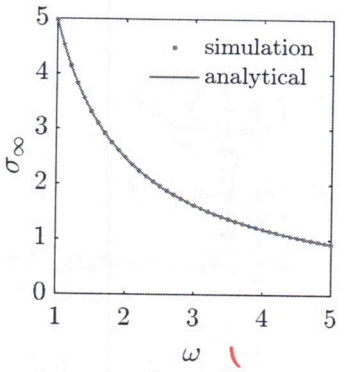

(b)

Figure 3.4: Comparison between the numerical and analytically derived results for (a) limiting standard deviation (σ_∞) versus the standard deviation of collapsed wavefunction (σ_M), and (b) limiting standard deviation (σ_∞) versus the natural frequency of the harmonic oscillator (ω).

In Fig. 3.4 the analytical result given by equation (3.10) is plotted with continuous lines while the numerical results are plotted with dots. In both these cases the theoretical results and simulation show good agreement.

3.6 Analysis

We found the limit distribution to be a Gaussian centered at zero with standard deviation given by equation (3.10) which can be simplified to

$$\sigma_\infty = \sqrt{\sigma_M^2 \cot^2 \omega t_M + \frac{\sigma_0^4}{4\sigma_M^2}}$$

We obtain a non-dimensional form by dividing throughout by σ_0,

$$\frac{\sigma_\infty}{\sigma_0} = \sqrt{\left(\frac{\sigma_M}{\sigma_0}\right)^2 \cot^2 2\pi \frac{t_M}{T} + \frac{1}{4}\left(\frac{\sigma_0}{\sigma_M}\right)^2}$$

or,

$$\varsigma^\infty = \sqrt{\varsigma_M^2 \cot^2 2\pi\tau_M + \frac{1}{4\varsigma_M^2}}$$

where $\varsigma^\infty = \frac{\sigma^\infty}{\sigma_0}$, $\varsigma_M = \frac{\sigma_M}{\sigma_0}$ and $\tau_M = \frac{t_M}{T}$. These substitutions are advantageous because they are dimensionless quantities independent of the length and time-scales of any particular harmonic oscillator.

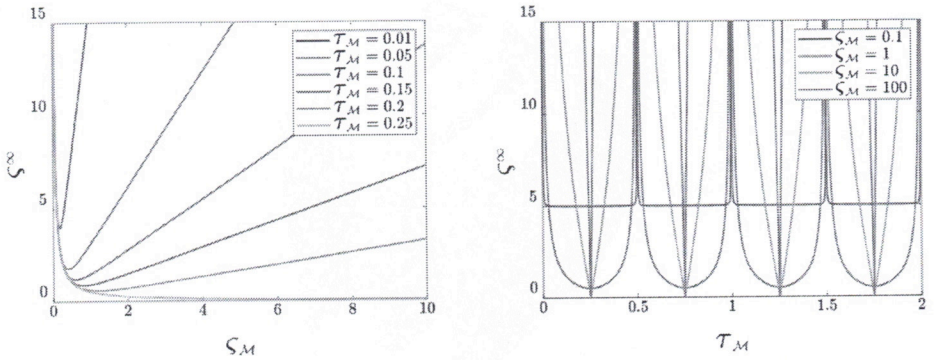

Figure 3.5: Plots of ς^∞ vs (a) ς_M and (b) τ_M. Color online.

In Fig. 3.5(a) we see how ς^∞ changes when we vary ς_M, for particular values of τ_M. For $\varsigma_M \to 0$, ς^∞ grows hyperbolically ($\sim \frac{1}{2\varsigma_M}$). It has a minimum value at $\varsigma_M = \sqrt{\frac{\tan 2\pi\tau_M}{2}}$. And as $\varsigma_M \to \infty$, it grows linearly in ς_M with slope $|\cot 2\pi\tau_M|$. For $\tau_M \in \left[0, \frac{1}{4}\right]$ the slope of the linear asymptote varies from ∞ to 0. After $\tau_M = \frac{1}{4}$, the process reverses itself till $\tau_M = \frac{1}{2}$, after which the pattern repeats periodically.

In Fig. 3.5(b) we see how ς^∞ changes with τ_M. The plots are periodic in τ_M with period $\frac{1}{2}$. The curves have minima at $\frac{n}{2} - \frac{1}{4}, n \in \mathbb{N}$. As ς_M increases ς^∞ gets steeper and the minima tend to zero.

In Fig. 3.6 the dependence of ς^∞ on both τ_M and ς_M have been consolidated into a single surface plot.

so with imprecise measurement the spread of the limiting distribution depends sensitively on the timing of the measurements, while for precise measurement $\varsigma^\infty \approx 1/\varsigma_M$ as long as $\tau_M \neq \frac{n}{2}$.

3.7 Conclusion

In this chapter, we have investigated the statistical distribution of periodic measurements on a single quantum system (in this case a quantum harmonic oscillator). We find that the measurement outcomes follow a Gaussian distribution with mean zero.

An analytical expression for the standard deviation of the limiting distribution was derived and was validated with numerical simulation. The standard deviation of this distribution was found to depend on the accuracy and frequency of measurements, and the natural frequency of the harmonic oscillator. This distribution was found to be independent of the initial wavefunction.

We have shown that there is an optimal accuracy of measurement that

precise msmt (small ς_M) produces a very narrow wave packet which will spread wide as long as $t_M \neq \frac{n}{2}$,
imprecise msmt (large ς_M) produces a wide wave packet that oscillates without spreading?

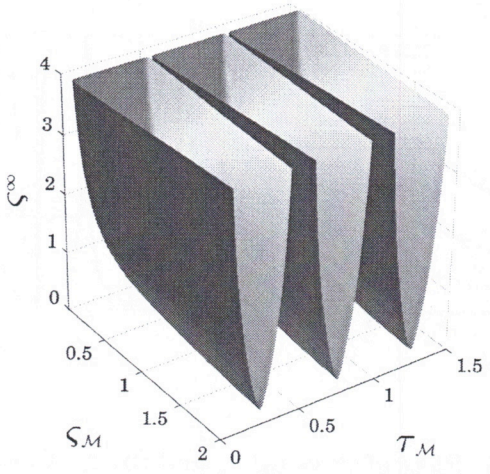

Figure 3.6: Plot of ς^∞ vs ς_M and τ_M

minimizes the standard deviation of the limit distribution. We also found that certain measurement intervals minimize the standard deviation of the limit distribution. The analytical results were numerically found to be robust to the presence of Gaussian noise in the time interval. These results may be useful for localizing a particle at the center of a well with the least uncertainty.

comment more here, there is a tradeoff in the value of ς^∞ and the precision of the timing:

very precise measurements can't get below $\varsigma^\infty \approx .5$ but the value of ς^∞ is not sensitive to t_M

while imprecise measurements can get close to $\varsigma^\infty \approx 0$ but rely on precisely timed measurements with $t_M = \frac{T}{4} + \frac{nT}{2}$

Chapter 4

Objective collapse due to a macroscopic object

> What exactly qualifies some physical systems to play the role of 'measurer'? Was the wavefunction of the world waiting to jump for thousands of millions of years until a single-celled living creature appeared? Or did it have to wait a little longer, for some better qualified system ... with a PhD? If the theory is to apply to anything but highly idealised laboratory operations, are we not obliged to admit that more or less 'measurement-like' processes are going on more or less all the time, more or less everywhere? Do we not have jumping then all the time?
>
> JOHN BELL
> Against 'measurement' [108]

4.1 Introduction

The collapse of the wavefunction is arguably the least understood process in quantum mechanics. The Copenhagen interpretation said that the process of measurement leads to an abrupt change in the wavefunction whereby it *collapses* into an eigenstate of the measured observable. Which physical processes constitute a measurement was left to the discretion of the practicing physicist. It is as if reality is brought to existence by the act of measurement. To resolve this unsatisfactory state of affairs, a plethora of ideas—

macro-micro divide, many worlds, and even consciousness—have been put forth. Contrary to the standard Copenhagen interpretation, objective collapse models modify the Schrödinger equation with nonlinear and stochastic terms in order to remove the act of conscious observation from the collapse process.

In this chapter we consider a macro-micro divide in a model system—the quantum version of a soft-impact oscillator—in which the possibility of interaction between a microscopic and a macroscopic object naturally arises. We propose a collapse model [130] in which macroscopic objects in the vicinity of a particle may stochastically collapse the wavefunction, without any intervention of a conscious observer. We investigate four possible conditions of such interaction-induced collapse and work out the experimentally testable predictions. We also describe an experiment where these predictions could possibly be tested.

is that the correct citation? That paper seems to relate to Ch. 3

4.2 The model system

Fig. 4.1 shows the classical analog of the system under consideration—a simple harmonic oscillator with mass m and spring constant k_1 which can impact with a wall, cushioned by a spring of constant k_2. The variable x is measured from the equilibrium position of the mass, and the wall is at x_w when the spring k_2 is relaxed.

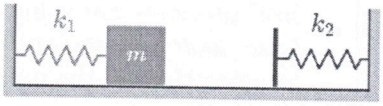

Figure 4.1: The classical soft-impact oscillator.

The classical system has been investigated in [240–242] with the inclusion of damping and external forcing, and under the condition of the wall being of negligible mass. It has been shown that such a system exhibits a sudden onset of chaos when the mass grazes the wall.

The quantum version of the above system will be a particle in a potential well, which is the same as the harmonic oscillator potential for $x \leq x_w$ and is given by a different parabolic function for $x \geq x_w$. The potential function of the system is given by

$$V(x) = \begin{cases} \frac{1}{2}k_1 x^2, & x < x_w \\ \frac{1}{2}k_1 x^2 + \frac{1}{2}k_2(x - x_w)^2, & x \geq x_w \end{cases} \tag{4.1}$$

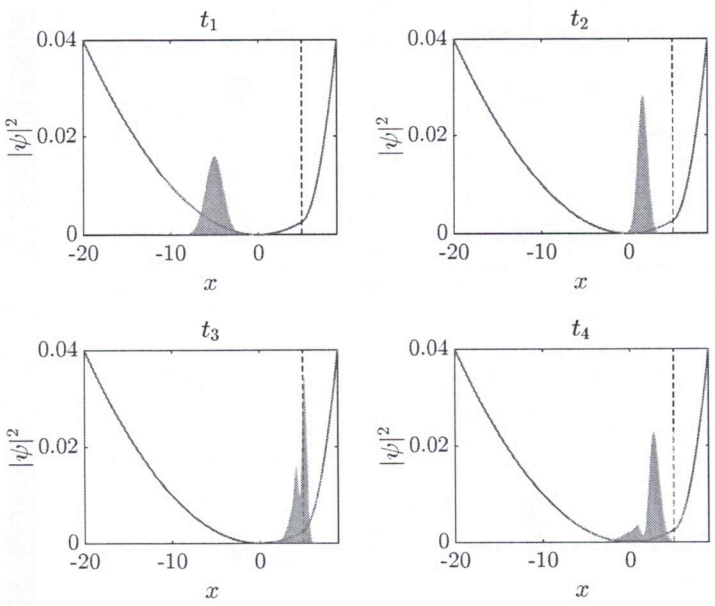

Figure 4.2: Evolution of the probability density distribution of the quantum particle at four time instants, with $t_1 < t_2 < t_3 < t_4$. Dashed line indicates the equilibrium position of the wall. The potential function, plotted in blue for the sake of visualization, is not to scale.

A Gaussian wavepacket centered at $x = -x_w$ is allowed to evolve according to the Schrödinger equation. Details of numerical simulation and parameter choices are given in Appendix 4.4.

Section? There are no Appendices

Fig. 4.2 shows snapshots of the dynamics of the probability density for this system. An animation of the evolution of the probability density function is given in supplementary material 1.

?? provide citation or link

To investigate the dynamics in the phase space, we compute the Wigner function

$$W(x,p) = \frac{1}{\pi\hbar}\int_{-\infty}^{\infty} \psi^*(x+y)\psi(x-y)e^{\frac{2ipy}{\hbar}}\,dy, \tag{4.2}$$

which gives a time-varying real valued function of the position and momentum. Fig. 4.3 shows the plots of the Wigner function in the x–p phase space at four different time instants. Prolonged observation of both $|\Psi|^2$ and the Wigner function shows that the time-evolution of the system is aperiodic.

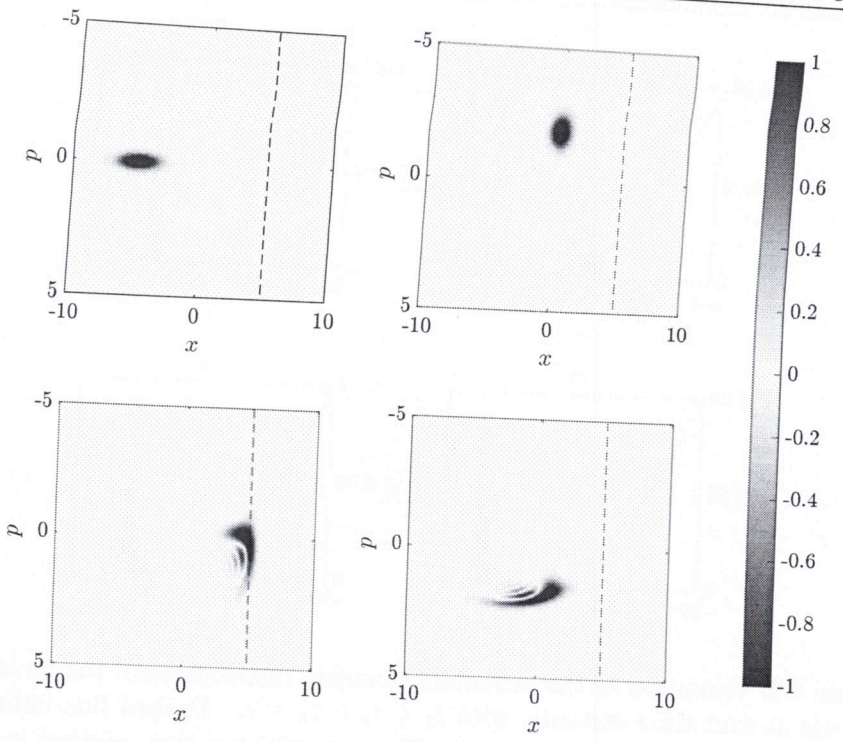

Figure 4.3: The evolution of the Wigner function at four time instants. The dashed line indicates the equilibrium position of the wall. The color denotes the value of the Wigner function.

4.3 Collapse!

In this section we bring in a new possibility. Since the wall can be considered to be a macroscopic object, an interaction of the particle with the wall (classically, an impact) may amount to a position measurement, which will cause the wavefunction to collapse (Fig. 4.4). Following a collapse, the wavefunction will continue to evolve according to the Schrödinger equation until the next collapse. Thus, if this possibility is considered, the evolution would contain unitary evolution as well as non-unitary collapse processes.

Unlike the classical impact oscillator, the impact of the particle with the wall will be a probabilistic event, guided by the pre-collapse wavefunction of the particle. However, the present knowledge does not allow us to pinpoint a unique algorithm with which the instant of collapse and the location of the collapsed wavefunction can be simulated. So we posit different postulates regarding the mechanism of collapse, and work out the implications of each.

Postulate 1: If the probability of finding the particle beyond the position

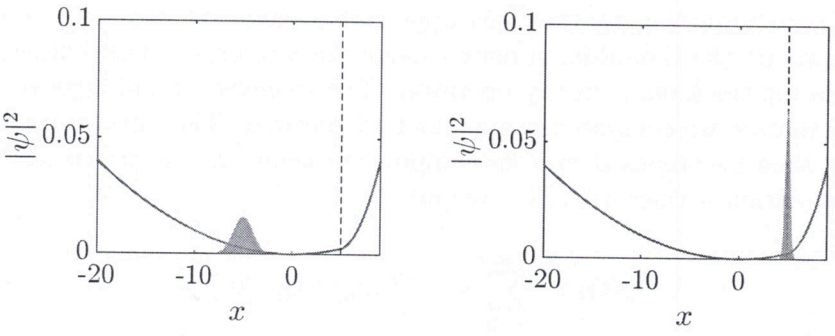

Figure 4.4: (a) Initial Gaussian with mean -5.0 and SD=1, (b) the post-collapse wavefunction—a narrow Gaussian located at the position of the wall $x = 5.0$ and SD=0.25. The potential function is shown in blue (not to scale).

of the wall exceeds a fraction r, i.e., if

$$\int_{x_w}^{\infty} |\psi(x)|^2 \mathrm{d}x \geq r, \qquad r \in (0, 1)$$

then the wavefunction collapses to the position of the wall.

Postulate 2: The same as Postulate 1, except that the number r is not fixed, and is a random number between 0 and 1. This implies that the time of collapse is also probabilistic, and the probability depends on the fraction of the probability distribution that lies beyond the wall.

Postulate 3: The same as Postulate 1, except that the wavefunction collapses to a point given by the pre-collapse probability distribution.

Postulate 4: The same as Postulate 2, except that the wavefunction collapses to a point given by the pre-collapse probability distribution.

Animations of the evolution of the probability density function for each of the postulates is given in supplementary material 2.

4.4 Numerical methods

We numerically solve the time-dependent Schrödinger equation for this system using the finite difference method by discretizing the range $[-30, 30]$ of the position basis into 1,500 segments. We make this choice after checking

that the wavefunction does not have appreciable magnitude beyond $x = \pm 30$. We construct the Hamiltonian matrix using the 8-th order central difference formula for the kinetic energy operator. The eigenvalues and eigenvectors of this matrix are computed using standard routines. The initial wavefunction is then decomposed into its components along the eigenvectors. The time-evolution is then trivial to compute

$$|\psi(t)\rangle = \sum_{n=0}^{N_{\text{cutoff}}} e^{-iHt/\hbar} |\phi_n\rangle \langle\phi_n|\psi(0)\rangle \tag{4.3}$$

For practical purposes, the infinite series is truncated at a cut-off energy such that the error is below machine precision. The first 150 eigenfunctions was found to be sufficient. We start from an initial wavefunction, which is a Gaussian wave-packet centered at $x = -5.0$, and standard deviation 1.0. This initial state corresponds, in the classical picture, to releasing the mass from the point $x = -5.0$, which would subsequently graze the wall located at $x = 5.0$. The other parameters are taken as $m = 1$, $k_1 = 1$, $k_2 = 10$. All quantities in this thesis are in units where $\hbar = 1$.

For the first and third collapse postulates, the value of r is taken as 0.5. The post-collapse wavefunction is supposed to be an eigenfunction of the position operator, i.e., a delta function. However, the numerical routine would not work with such discontinuous functions. So we consider the post-collapse wavefunction to be a narrow Gaussian function of standard deviation 0.25 (Fig. 4.4). At the instant of collapse, the wavefunction is replaced with the collapsed wavefunction at the position dictated by the respective postulate. This is then decomposed into the energy eigenfunctions and its evolution is calculated using equation 4.3. The parameter values are taken as: mass of the quantum particle $m = 1$, spring constant of the spring attached to the mass $k_1 = 1$, the spring constant corresponding to the soft wall $k_2 = 10$, time step $\delta t = 0.1$. We calculate for a total number of 10,000 timesteps. In the case of the classical ensemble, 10,000 particles are initialized with zero velicity and positions drawn from a normal distribution with mean -5 and standard deviation 1. The dynamics is simulated using the classical equations of motion and integrated using the Runge–Kutta–Fehlberg method.

4.5 Results

Our objective here is to obtain testable predictions of the various possible mechanisms of evolution of the wavefunction as outlined above. We focus on two observables: energy and position.

4.5.1 Probability distribution of energy values

An energy measurement may return any energy eigenvalue, but the probability of finding each eigenvalue would be different for various postulated situations. For the different postulates, the computed probability distribution of the energy eigenvalues are presented in Fig. 4.5 and the expectation values of energy are tabulated in Table 4.1. These results are compared to the predictions of quantum mechanics without collapse and to the situation in the classical impact oscillator. The classical ensemble considered has the same initial distribution in position as given by the initial wavefunction for the other cases.

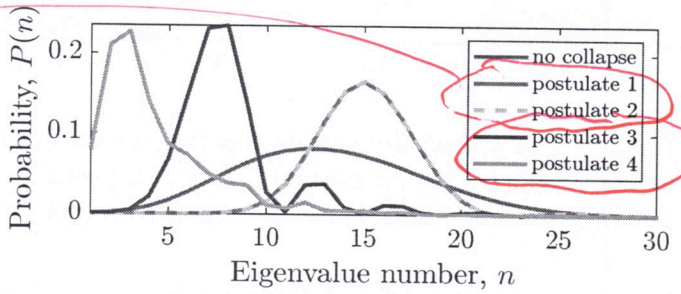

Figure 4.5: Comparison of probability distributions for energy eigenvalues for the different cases.

Postulate	Expected energy
No collapse	13.125 GeV
Postulate 1	14.75 GeV
Postulate 2	14.62 GeV
Postulate 3	11.46 GeV
Postulate 4	5.57 GeV
Classical ensemble	13.0005

Table 4.1: Expectation values of energy in the four postulated situations along with the predictions of quantum mechanics and the classical case.

Note that the expectation value of energy (Table 4.1) for unitary evolution of the wavefunction depends on the initial wavefunction considered, and those for the four collapse postulates depend on the variance of the post-collapse wavefunction. Since we have considered the standard deviation to be 0.25 in all cases, one should pay attention to the relative magnitudes rather than the absolute magnitudes of the expectation values.

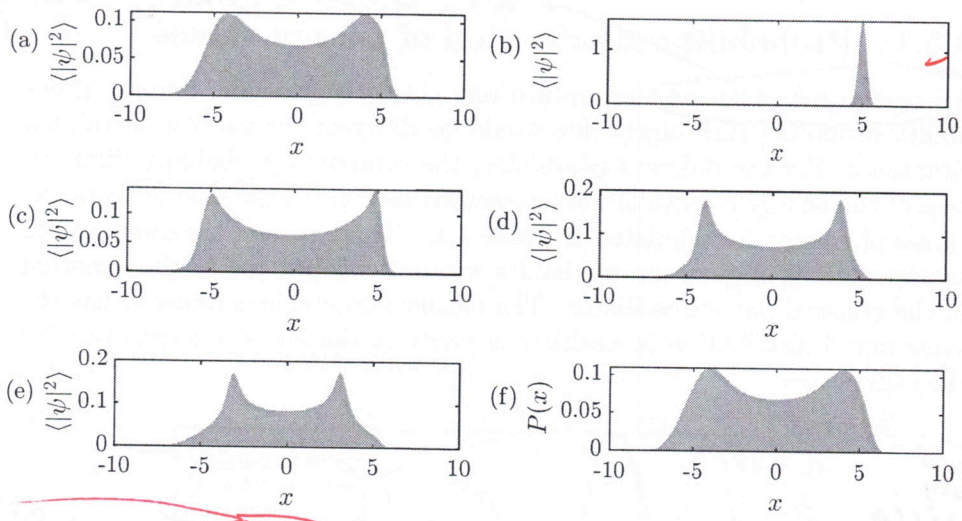

I don't see how this can be correct

Figure 4.6: The averaged probability density functions of the position of the particle (a) without collapse, (b) for postulate 1, (c) for postulate 2, (d) for postulate 3, (e) for postulate 4 and (f) for the classical ensemble.

time averaged? over what time span? I don't understand what you are averaging over.

The results presented in Fig. 4.5 and Table 4.1 show that, if experiments give the expectation value of energy larger than what is predicted by standard quantum mechanics for this system, then Postulate 1 or 2 may be true, and if they give a lower value, Postulate 3 or 4 may be true. The probability distribution of energy for unitary evolution without collapse is found to be in close agreement with the classical ensemble.

4.5.2 Probability distribution of position values

We have computed the distribution of position values obtained through 10,000 time-steps. These are plotted in Fig. 4.6.

It is found that if Postulate 1 is true, there is only one peak in the probability distribution and in all other cases there are two peaks. For unitary evolution without collapse and for the classical ensemble, the two peaks are of almost the same height while in the other cases they are of dissimilar heights. Table 4.2 gives the mean and standard deviation of the distributions for the six cases shown in Fig. 4.6. The expected position of the particle in the case of no collapse and postulate 2 are closest to the predictions of classical mechanics.

I don't understand Fig. 4.6 and Table 4.2 at all.

The distribution of collapse locations for postulates 1 and 2 are trivial, as they always collapse at the location of the wall. The distributions for postulates 3 and 4 are plotted in Fig. 4.7. The distributions are almost

Are these time averages over $t \in [0, t_c]$ where t_c is the time of collapse? Or are these averages over many collapses of $|\psi|^2$ at the instant collapse is triggered? or something else?

this seems the most plausible to me, but it is not at all clear

but then 3 should be same as 1

I'm confused!

Postulate	Mean	SD
No collapse	-0.2662	3.4963
Postulate 1	4.8217	1.1296
Postulate 2	-0.2630	3.6354
Postulate 3	-0.0657	3.1330
Postulate 4	-0.0812	2.8818
Classical ensemble	-0.1984	3.4991

Table 4.2: Mean and standard deviations of the time averaged PDFs for the different collapse postulates.

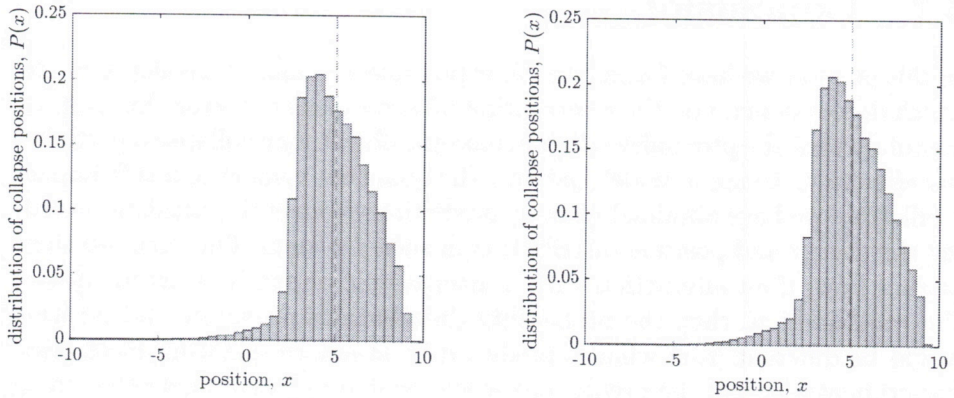

Figure 4.7: Distribution of collapse locations in (a) postulate 3 and (b) postulate 4.

identical. This implies that the difference between these two postulates has negligible effect on the long term dynamics.

Among the postulates considered, postulate 2 is the most plausible one as it has the best correspondence with the results of the classical theory.

4.6 Possible experimental tests

At present all four postulates remain possibilities, and only experimental tests can eliminate the wrong ones. Supercooled nanomechanical cantilevers, used in atomic force microscopy, is one candidate system where these predictions could be tested.

The tip dynamics of the cantilever can be modeled [243–245] as an impact oscillator at the transition point between attractive and repulsive tip-sample

interactions [246]. Experimental tests into these systems have confirmed the onset of chaos due to grazing bifurcations [247], similar to what is observed in the impact oscillator.

Advances in laser cooling have made cooling these nano-mechanical systems to their ground state a distinct possibilty [248]. Protocols for creation and verification of superposition [249], and entanglement [250] between two nanocantilevers, have been proposed. It may be possible to perform measurements for the distribution of the position values [251], and thus the postulates could be tested.

4.7 Conclusion

In this chapter we have formulated four possible variants of a collapse model which do not depend on the intervention of a conscious observer. Instead, we postulate that the proximity to a macroscopic object may collapse a particle's wavefunction. Using a model system—the quantum version of a soft-impact oscillator—we have obtained testable predictions from each postulate regarding the energy and position distribution in such a system. Our computations predict that, if an interaction with a macroscopic object induces collapse of the wavefunction, then the probability distributions of energy and position would be different from what is predicted by standard quantum mechanics. Experimental test of the predictions would enable us to eliminate the wrong postulates.

Chapter 5

Conclusions

This thesis is a multifaceted exploration of quantum dynamics, collapse mechanisms, and measurement statistics, shedding light on novel aspects of quantum behavior. Our findings contribute to the ongoing quest for a deeper understanding of the nature of quantum systems.

We investigated the quantum dynamics of a non-smooth classical system, the impact oscillator. In the absence of forcing and damping, the classical oscillator undergoes periodic motion. Upon sinusoidal forcing beyond a critical amplitude, the system transitions to a large amplitude chaotic orbit at the grazing condition (ie. zero velocity impacts with the wall).

On the quantum side, the system shows quasiperiodic behavior in the absence of forcing. When a sinusoidal drive is added, the Floquet quasienergy spectrum transitions from Poisson to Gaussian unitary ensemble as the amplitude of the driving is increased. In order to study the dynamical features, we transformed the evolution of the complex-valued wavefunction into a real-valued time series by calculating its entropy and L_1-norm and applied standard diagnostic techniques to these time series. We uncovered a new form of aperiodic evolution around the classical grazing condition, exhibiting signatures of strange nonchaotic dynamics. This form of dynamics, usually observed in quasiperiodically forced classical systems, gives rise to a strange (geometrically fractal) attractor but does not have a sensitive dependence on initial conditions.

and damped, otherwise you don't get an attractor

Inspecting the extracted time series, we found that its frequency spectrum was discrete but dense, which is a characteristic feature of strange attractors [79, 252]. The distribution of local Lyapunov exponents had a positive component while the global Lyapunov exponent was negative, indicating that the global dynamics was contracting but there were local instabilities, as is characteristic of strange nonchaotic dynamics. The spectral distribution function had power law character and the 0-1 test converged to values be-

tween 0 and 1. All results pointed to the fact that the underlying dynamics was strange but not chaotic. To our knowledge, this is the first instance of strange nonchaotic dynamics in a quantum system.

Measurement outcomes in quantum mechanics are inherently random. For identically prepared quantum systems, Born's rule tells us that the distribution of measurement outcomes should match the square of the amplitude of the wavefunction when each system is measured exactly once. In contrast, we were interested in the statistics of periodic measurements in a single quantum system. For this study, we chose the quantum harmonic oscillator as our test-bed and subjected it periodically to measurements by an unsharp instrument. The harmonic oscillator was chosen because of its ubiquity, as it approximates the dynamics near the minima of any smooth potential well; as well for its analytical tractibility. We showed that in the limit of infinite measurements with an instrument of finite precision, the distribution of outcomes converges on a zero-mean Gaussian function. We derived the expression for the standard deviation of the distribution

$$\sigma_\infty = \sqrt{\sigma_{\mathcal{M}}^2 \cot^2 \omega t_{\mathcal{M}} + \frac{\sigma_0^4}{4\sigma_{\mathcal{M}}^2}}$$

Where ω is the natural angular frequency of the oscillator, σ_0 is the ground-state width, $t_{\mathcal{M}}$ is the time between consecutive measurements and $\sigma_{\mathcal{M}}$ is the standard deviation of the measurement profile, which is a measure of the precision of the measuring instrument. We validated that the analytical results are robust to perturbations by introducing noise into the parameters of the model in numerical experiments. This work identified the optimal measurement parameters for minimizing the standard deviation of measurement outcomes of a particle in a harmonic trap. These results have practical implications for localizing particles with minimal uncertainty.

Objective collapse models provide a testable solution to the quantum measurement problem. By positing that the wavefunction collapses spontaneously, they take the conscious observer out of the measurement process. The collapses are considered perfectly acausal in such models. We, on the other hand, explored objective collapse causally mediated by a macroscopic object. We proposed four variants of a collapse model that do not require the intervention of a conscious observer but instead rely on the proximity to macroscopic objects.

In a soft impact oscillator, the wall can be treated as a macroscopic object. The fraction of the wavefunction penetrating the wall (call it p_{wall}) was taken as the interaction strength with the wall and consequently the causal factor for the collapse. We considered the following possibilities regarding

the deterministic or stochastic influence of p_{wall} (viz. when to collapse?)

A. p_{wall} causes a collapse the instant it exceeds a critical value

B. p_{wall} is the probability of collapse at any instant

and the following possibilities about the location of the collapse (viz. where to collapse?)

C. the wavefunction always collapses at the position of the wall

D. the wavefunction collapses following Born's rule.

We investigated all four combinations of the above possibilities, numbering them as (1) AC, (2) AD, (3) BC, and (4) BD. The time-averaged probability distribution in position was calculated to distinguish between the four cases. It had a single peak in case 1 while it was double-peaked in all the other cases. The two peaks were not symmetric. Cases 1 and 2 produce identical distribution in energy while the other two cases are distinct. The location of collapse could vary in only cases 3 and 4, where we found that the distribution of collapse locations in both cases are almost identical, implying that the nature of the wall's influence, whether deterministic or stochastic, has little observable effect. The computations provided testable predictions for the energy and position distributions, highlighting potential deviations from standard quantum mechanics. Experimental validation of these predictions would offer valuable insights into the nature of collapse mechanisms.

I still don't understand that.

Collectively, this research work extends our understanding of quantum dynamics, collapse mechanisms, and measurement statistics. The observed strange nonchaotic behavior in the impact oscillator opens up new avenues for exploring quantum phenomena and holds potential applications in quantum information and related technologies. The proposed collapse models and the challenges they pose to conventional interpretations of wavefunction collapse provide valuable insights into the foundations of quantum mechanics. Additionally, the statistical analysis of quantum measurements contributes to our ability to manipulate and control quantum systems with greater precision.

5.1 Scope of future work

We studied the dynamics of the driven quantum impact oscillator in the quantum limit. Our work provided numerical evidence for strange nonchaotic

features in the time series extracted from the quantum dynamics. Further work is needed for the analytical justification of our claims. Secondly, most studies on the classical impact oscillator consider the damped-driven case. The presence of dissipation gives rise to a strange chaotic attractor in the classical system. It remains to be seen what this would imply in the quantum limit.

Despite their success, most of the objective collapse models—Ghirardi-Rimini-Weber (GRW) [134], Continuous Spontaneous Localisation (CSL) [135] and Diosi-Penrose (DP) [253]—suffer from energy non-conservation. Although a partial resolution to the problem has been found by introducing dissipation [254, 255], it raises new questions about the origin and nature of the noise field considered. Hence, it is an avenue for further research.

While our findings provide evidence for the existence of novel dynamics and the need for alternative collapse mechanisms, further investigations and experimental tests are needed to fully validate and understand these phenomena. We have identified a system that allows for testing these results. When the nanomechanical cantilever used in atomic force microscopy is supercooled, its tip dynamics should begin to display quantum behavior, as has been suggested in numerous studies. Advances in laser cooling have made realizing such a system a distinct possibility. From a classical standpoint, this system can be represented as an impact oscillator at the point where the tip interactions transition from attractive to repulsive. This presents an ideal experimental opportunity to validate our findings.